Remote Sensing of Environment 129 (2013) 262–279

Contents lists available at SciVerse ScienceDirect

Remote Sensing of Environment

journal homepage: www.elsevier.com/locate/rse

A sub-pixel-based calculation of fire radiative power from MODIS observations: 1 Algorithm development and initial assessment

David Peterson [a,*], Jun Wang [a], Charles Ichoku [b], Edward Hyer [c], Vincent Ambrosia [d]

[a] University of Nebraska, Lincoln, Lincoln, NE 68588, USA
[b] NASA Goddard Space Flight Center, 8800 Greenbelt Road, Greenbelt, MD 20771, USA
[c] Naval Research Laboratory, 7 Grace Hopper Avenue, Monterey, CA 93940, USA
[d] NASA-Ames Research Center, Mail Stop 245-4; Room 128, Moffett Field, CA 94035-0001, USA

ARTICLE INFO

Article history:
Received 4 December 2011
Received in revised form 8 September 2012
Accepted 26 October 2012
Available online 11 December 2012

Keywords:
Fire
Wildfire
Biomass burning
Fire radiative power (FRP)
MODIS
Fire area
Fire temperature
Sub-pixel
Fire detection
Airborne

ABSTRACT

Developed as a quantitative measurement of fire intensity, fire radiative power (FRP) and the potential applications to smoke plume injection heights, are currently limited by the pixel resolution of a satellite sensor. As a result, this study, the first in a two-part series, develops a new sub-pixel-based calculation of fire radiative power (FRP_f) for fire pixels detected at 1 km^2 nominal spatial resolution by the MODerate Resolution Imaging Spectroradiometer (MODIS) fire detection algorithm (collection 5), which is subsequently applied to several large wildfire events in California. The methodology stems from the heritage of earlier bi-spectral retrievals of sub-pixel fire area and temperature. However, in the current investigation, a radiative transfer model is incorporated to remove solar effects and account for atmospheric effects as a function of Earth-satellite geometry at 3.96 and 11 μm (MODIS fire detection channels). The retrieved sub-pixel fire (flaming) area is assessed via the multispectral, high-resolution data (3–50 m) obtained from the Autonomous Modular Sensor (AMS), flown aboard the NASA Ikhana unmanned aircraft. With fire sizes ranging from 0.001 to 0.02 km^2, pixel-level fire area comparisons between MODIS and AMS are highly variable, regardless of the viewing zenith angle, and show a low bias with a modest correlation (R = 0.59). However, when lower confidence fire pixels and point-spread-function effects (fire hot spots on the pixel edge) are removed, the correlation becomes much stronger (R = 0.84) and the variability between MODIS and AMS is reduced. To account for these random errors via averaging, two clustering techniques are employed and the resulting AMS and MODIS comparisons of fire area, after correcting for overlapping MODIS pixels, are even more encouraging (R = 0.91). Drawing from the retrieved fire area and temperature, the FRP_f is calculated and compared to the current MODIS pixel area-based FRP. While the two methods are strongly correlated (R = 0.93), the FRP_f, in combination with retrieved fire cluster area, allows a large fire burning at a low intensity to be separated from a small fire burning at a high intensity. Similarly, the flux of FRP_f over the retrieved fire area can be calculated, allowing for improved estimates of smoke plume injection heights in modeling studies and creating potential applications for the future VIIRS and GOES-R fire detection algorithms.

© 2012 Elsevier Inc. All rights reserved.

1. Introduction

Observed in many regions of the globe, biomass burning is a key component to the Earth-atmosphere system, climate change, and operational forecasts of meteorology and air quality. Individual fires are ignited by natural causes, such as lightning strikes (e.g. Peterson et al., 2010) and anthropogenic causes, such as agriculture and forest clearing (e.g. Koren et al., 2007; van der Werf et al., 2008). Regardless of cause, these fires subsequently burn large tracts of land across the globe every year. For example, Roy et al. (2008) estimated that nearly 3.7 million square kilometers burned globally from July 2001 to June 2002. Wildfires also create concerns for air quality by releasing enormous amounts of aerosols and trace gases into the atmosphere (e.g. Jordan et al., 2008; Spracklen et al., 2007). Above the boundary layer, smoke particles can be transported thousands of miles (e.g. Duck et al., 2007; Sapkota et al., 2005) creating health concerns and interacting with meteorological processes a great distance from a fire (e.g. Wang et al., 2006). In some cases, wildfires can even generate pyroconvection, which has been shown to inject smoke aerosols and trace gasses into the upper troposphere and even into the stratosphere (Fromm et al., 2010). In addition, deposition of fire-generated black carbon particles on ice sheets has been shown to reduce the surface albedo causing atmospheric warming and increased melting (Kopacz et al., 2011; Randerson et al., 2006).

* Corresponding author at: University of Nebraska, Lincoln, Department of Earth and Atmospheric Sciences, 130 Bessey Hall, Lincoln, NE 68588, USA. Tel.: +1 219 742 2613.
E-mail addresses: david.peterson@huskers.unl.edu (D. Peterson), jwang7@unl.edu (J. Wang), charles.m.ichoku@nasa.gov (C. Ichoku), edward.hyer@nrlmry.navy.mil (E. Hyer), vincent.g.ambrosia@nasa.gov (V. Ambrosia).

0034-4257/$ – see front matter © 2012 Elsevier Inc. All rights reserved.
http://dx.doi.org/10.1016/j.rse.2012.10.036

Over the past three decades, several satellite sensors have been able to provide observations of fire locations at different spatial scales and temporal frequencies. These include the NOAA Advanced Very High Radiometer (AVHRR), Geostationary Orbiting Environmental Satellite (GOES), Advanced Spaceborne Thermal Emission and Reflection Radiometer (ASTER), and the MODerate Resolution Imaging Spectroradiometer (MODIS). Some of these sensors also map burned areas. Among these sensors, MODIS is especially important because (1) MODIS has the highest saturation temperature of ~500 K at its 4 μm fire detection channel (Gao et al., 2007; Justice et al., 2002; Kelha et al., 2003), which allows a high percentage of detected fires to be characterized through fire radiative power (FRP) — a quantitative measure of fire intensity (Kaufman et al., 1998a), and (2) the twin MODIS sensors aboard the Terra (launched in 1999) and Aqua (launched in 2002) satellites allow wildfires to be observed globally up to four times each day; twice in the daytime and twice at night.

Even though a large region may be burned by a fire over its lifetime, only a portion of the burn area is actually in flames (fire front) at any given observation time (Kaufman et al., 1998a; Lee & Tag, 1990). Despite much advancement in fire remote sensing during the last couple of decades, all satellite sensors, including MODIS, provide fire locations as pixels that are flagged as containing fires. Unfortunately, the pixel resolution is usually too coarse to resolve the size of small fire hot spots that may be very intense relative to large but low-intensity fires. In fact, recent research indicates that FRP can be used as a quantitative indicator for fire intensity and is proportional to both the fire's fuel consumption and smoke emission rates (e.g. Ichoku et al., 2008a, 2008b; Ichoku & Kaufman, 2005; Jordan et al., 2008; Roberts et al., 2009, 2005; Wooster, 2002, Wooster et al., 2003, 2005). Direct derivation of smoke emission from satellite-based FRP can overcome the spatial errors in the traditional estimate of fire emission in which the variation of land surface types within the sensor pixel plays an important role (Hyer & Reid, 2009). Val Martin et al. (2010) further show that regions of intense burning (high FRP) commonly result in higher altitude smoke plumes and a greater chance of smoke transport into the free troposphere. However, similar to fire detections, the primary drawback for current MODIS FRP data is that they are estimates of fire radiative power released over a pixel area. In reality, it is the rate of energy release over the fire area (the fire intensity (Byram, 1959)) that is directly related to the thermal buoyancy (Kahn et al., 2007; Lavoue et al., 2000), which influences the smoke injection height and the transport of smoke plumes into the free troposphere. Therefore, an accurate retrieval of fire intensity would be a valuable addition to the current suite of satellite fire products.

Many early studies could not validate the results of sub-pixel retrievals due to the dearth of suitable data sources (e.g. Dozier, 1981). However, multispectral, high-resolution data (3–50 m), obtained from the airborne Autonomous Modular Sensor (AMS) are now available for numerous fire events in the western United States (e.g. Ambrosia & Wegener, 2009). In many cases, the AMS flight scan can be spatiotemporally collocated with MODIS scenes (Fig. 1), allowing for an unprecedented representation of the flaming, smoldering, and background regions within a given MODIS fire pixel. By using the collocated data, a quantitative assessment of a MODIS sub-pixel retrieval of fire information can be conducted for multiple fire events in various biomes. The AMS data can also be used to validate background temperatures and to isolate the various sources of error known to affect sub-pixel retrievals.

As shown in several studies (e.g. Giglio & Kendall, 2001), many variables must be considered when developing and assessing the accuracy of a sub-pixel fire retrieval. Therefore, this study is the first in a two-part series, and focuses primarily on: (1) developing an algorithm to retrieve sub-pixel fire information for MODIS with atmospheric and daytime solar effects taken into consideration, (2) demonstrating the usefulness of an AMS-derived fire (hot spot) detection algorithm to assess the results of the sub-pixel fire area from MODIS and (3) calculating the sub-pixel-based FRP. Subsequent sections of this paper describe the current MODIS FRP, the need for a sub-pixel retrieval in the context of FRP calculations, the history of sub-pixel retrieval methodologies, and the specifics of a modified MODIS sub-pixel retrieval methodology. Results are shown from the comparison of MODIS retrieval fire area with AMS observations and comparisons between the MODIS and sub-pixel-based FRP for several fire events occurring between August and October 2007. A detailed theoretical sensitivity analysis of the sub-pixel retrieval algorithm's uncertainty, including a case study application, will be presented in part 2 of this series.

2. The need and method for a sub-pixel-based calculation of FRP

In contrast to earlier sensors, MODIS is currently the only operational satellite sensor designed to specifically measure FRP globally (e.g. Ichoku et al., 2008a; Kaufman et al., 1998a, 1998b). Prior to MODIS collection 5 data, the MODIS fire detection algorithm retrieved FRP with respect to the individual pixel areas, or in units of Watts per pixel area (Kaufman et al., 1998a). In collection 5, FRP is multiplied by the pixel area (FRP_p), and is provided in units of Megawatts. Specifically, the FRP_p calculation employs a best-fit equation for a wide variety of fire simulations and is calculated for all fire pixels (top-of-atmosphere) using only the 4 μm channels:

$$FRP_p = 4.34 \times 10^{-19}\left(T_4^8 - T_{4b}^8\right)A_p \tag{1}$$

where T_{4b} is the background brightness temperature (in K), T_4 is the brightness temperature of the fire pixel, and A_p is the area of the pixel (Giglio, 2010; Kaufman et al., 1998a, 1998b, 2003). Therefore, FRP_p in collection 5 is a function of satellite viewing zenith angle. Regardless of the version of data collections, FRP_p can be used for estimating the total radiation from the fire, and consequently, can be related to the total amount of trace gases and particles emitted by the fire, which is useful for mesoscale modeling with a large model grid (e.g. Wang et al., 2006). In addition, FRP_p is being used for near real-time emission maps at a global scale (Kaiser et al., 2009).

While the use of FRP_p for estimating the fire emissions is well recognized (Vermote et al., 2009), its potential use for other applications, such as estimating smoke injection heights and fire intensity, is limited by the lack of sub-pixel information for fires (Eckmann et al., 2010). This can be understood via a simple example in which the FRP_p value is equal for two pixels covering the same area, but containing different burning scenarios: (1) a large fire with burning at a low intensity or (2) a small fire burning at a high intensity. Not surprisingly, a large difference in fire behavior and the thermal buoyancy to drive the rise of smoke plumes can be expected between (1) and (2). However, it will not be discernable in the current MODIS FRP_p product unless sub-pixel information of fire area and temperature is retrieved.

In contrast to the current MODIS FRP_p calculation (Eq. 1), retrieved sub-pixel data would allow for a direct fire area and temperature-based calculation of FRP for each sub-pixel fire (FRP_f). Similar to Zhukov et al. (2006), the FRP_f equation (units of Megawatts, above the mean background) uses the Stefan–Boltzmann relationship in the 4 μm channel

$$FRP_f = \sigma\left(T_f^4 - T_{4b}^4\right)A_f \tag{2}$$

where σ is the Stefan–Boltzmann constant (5.6704×10^{-8} W m^{-2} K^{-4}), T_f is the retrieved kinetic fire temperature at the surface (not the pixel temperature), T_{4b} is the background brightness temperature, and A_f is the retrieved fire area. At cool 4 μm temperatures, atmospheric effects, especially from water vapor content, are minor, which allows T_{4b} to be used as an approximation of surface kinetic background temperature (Kaufman et al., 1998a, also explored in part 2 of this series). While each FRP method is different for the same fire, the FRP_f (fire area and temperature-based FRP), in theory,

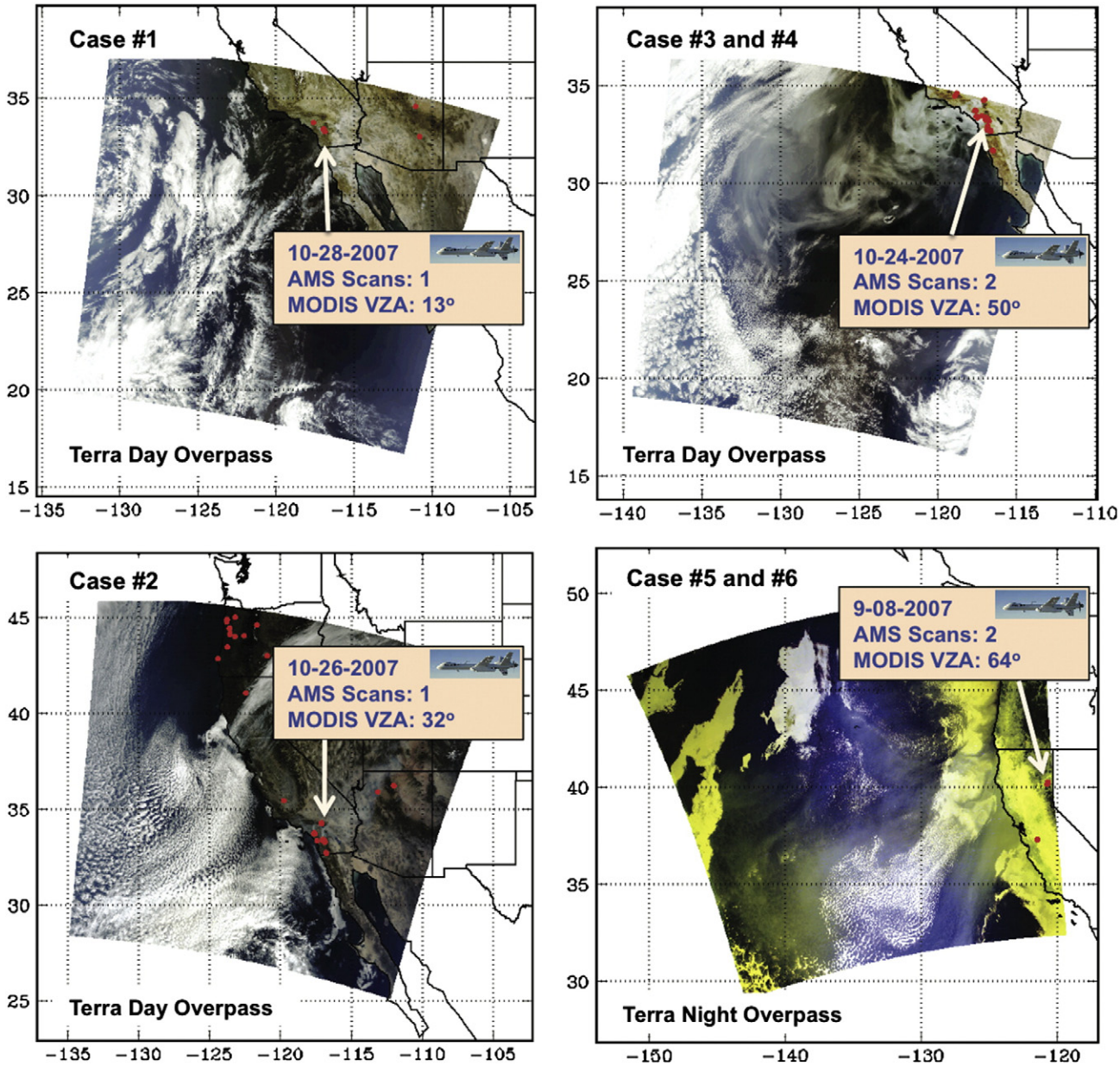

Fig 1. Projections of the four MODIS scenes that contain the six AMS flight scans (details provided in Table 1). Red dots denote the locations of MODIS fire pixels (not to scale) and arrows highlight the fire pixels that are collocated with at least one AMS scan. While two collocations may come from the same MODIS scene, steps are taken to minimize overlap.

should be strongly correlated to the pixel-based FRP_p value. This assumption can be used because at 4 μm, the radiative power from flaming usually overwhelms that from smoldering within any MODIS pixel (Kaufman et al., 1998a). However, an exact match is not likely because FRP_p (Eq. 1) is based on a best-fit curve from theoretic simulations of many sub-pixel fire scenarios, including variations in fire temperature, fire area, and smoldering or flaming regions. FRP_p also disregards the atmospheric attenuation of infrared radiation, and hence may contain relatively large uncertainties for individual fire events (Kaufman et al., 1998a).

3. Sub-pixel retrievals of fire area and temperature

Dozier (1981) made the first attempt to derive a sub-pixel fire (target) retrieval using a bi-spectral approach. This "Dozier" method uses the spectral contrast between a sub-pixel hot target and the surrounding (presumably uniform) background of the pixel for the 3.8 μm middle infrared (MIR) and 10.8 μm thermal infrared (TIR) channels. Although originally developed for the AVHRR, the Dozier method, in principle, can be applied to any sensor having similar MIR and TIR channels. Using MODIS fire detection as an example, the calculation is performed for each wavelength used in fire detection (~4 and 11 μm) providing two equations that can be solved for the fire temperature (T_f) and the fractional area of the pixel covered by the fire (P), where $0<P<1$, located within a uniform background at temperature T_b (surface kinetic temperature). The observed radiances at 4 and 11 μm (top-of-atmosphere), denoted by L_4 and L_{11}, respectively, are

$$L_4 = PB\left(\lambda_4, T_f\right) + (1-P)B(\lambda_4, T_b) \tag{3}$$

$$L_{11} = PB(\lambda_{11}, T_f) + (1-P)B(\lambda_{11}, T_b) \tag{4}$$

where $B(\lambda,T)$ is the Planck function and T_b is estimated from a temperature dataset. The fire (hot target) and background are assumed to be blackbodies with unit emissivity in both channels (Giglio & Kendall, 2001). In addition, all atmospheric effects are neglected, allowing the computation of $B(\lambda,T)$ to be considered a top-of-atmosphere value. With these assumptions, the surface kinetic temperatures, T_f and T_b, can be considered as brightness temperatures and can be used for both channels; otherwise Eqs. (3) and (4) are not valid.

Due to the small size of sub-pixel fires and the lack of high spatial and high thermal resolution data, the original Dozier retrieval is hard to validate. Nevertheless, it was applied to several satellite sensors between 1981 and 2000 (e.g. Flannigan & Vonder Haar, 1986; Green, 1996; Langaas, 1993; Matson & Dozier, 1981; Prins & Menzel, 1992; Riggan et al., 1993), and an extensive historical review from this period can be found in Giglio and Kendall (2001). The following sections highlight the modifications to the Dozier method over the last decade with a focus on the uncertainty analysis and challenges for validation. This is subsequently followed by the description of the sub-pixel implementation and initial assessment specific to this study.

3.1. Previous modifications and analysis of sub-pixel retrievals

Not surprisingly, the assumptions used in the original Dozier retrieval can be unrealistic. For example, atmospheric effects, such as water vapor content, undoubtedly have a major impact on the retrieval, and the fire and background are not blackbodies. Therefore, to create a more realistic retrieval, several studies modified the retrieval by adding relevant terms to the equations (e.g. (Giglio & Kendall, 2001; Prins & Menzel, 1992). With these modifications, the observed radiances at 4 and 11 μm, respectively, are

$$L_4 = \tau_4[PB(\lambda_4, T_f) + e_{4b}(1-P)B(\lambda_4, T_b) + (1-P)(1-e_{4b})I_{4ref}] \quad (5)$$

$$L_{11} = \tau_{11}[PB(\lambda_{11}, T_f) + e_{11b}(1-P)B(\lambda_{11}, T_b)] \quad (6)$$

where e_{4b} and e_{11b} respectively denote the background emissivity at 4 and 11 μm, I_{4ref} is the reflected solar radiance in the 4 μm channel at the surface (equal to zero at night), and τ_4 and τ_{11} are the upward MIR atmospheric transmittance and the upward TIR atmospheric transmittance, respectively. The relationships in Eqs. (5) and (6) contain several unknowns, and therefore require the aid of a radiative transfer model. The emissivity of the fire is commonly assumed to be equal to one (e.g. Giglio & Kendall, 2001), which has been shown to be a reasonable assumption for most fire events with thick fire fronts. As a result, Eqs. (5) and (6) do not include emissivity in the fire term.

By assuming identical surface and atmospheric conditions, the MODIS fire product estimates background brightness temperatures (or radiances at the top-of-atmosphere) for the 4 and 11 μm channels by averaging several neighboring, fire-free pixels (Giglio et al., 2003; Justice et al., 2002). These background radiances, denoted by L_{4b} and L_{11b}, can be expressed respectively, as

$$L_{4b} = \tau_4[e_{4b}B(\lambda_4, T_b) + (1-e_{4b})I_{4ref}] \quad (7)$$

$$L_{11b} = \tau_{11}e_{11b}B(\lambda_{11}, T_b). \quad (8)$$

Substituting Eqs. (7) and (8) into Eqs. (5) and (6) will create a simplified version of Eqs. (5) and (6), where P and T_f are the only unknown variables. Therefore, fire fraction and fire temperature can be retrieved simultaneously from a combined use of the MODIS-observed background and fire pixel radiances.

Even with improved calculations, two distinct hindrances to the Dozier retrieval have become obvious: (1) the validation difficulty and (2) the potential sources for error in the retrieval. For proper validation, the sensor providing the 'ground truth' must do so at a relatively fine spatial resolution and the observation time must be very close to that of the satellite sensor under scrutiny. Unfortunately, such measurements are typically not available in sufficient quantities to accomplish a significantly representative validation. While the validation issues are relatively straight forward, understanding the potential for error is much more complex. Sources of error may include band-to-band coregistration issues, improper selection of background temperature and atmospheric transmittance, instrument noise, varying sub-pixel proportions of flaming, smoldering, and unburned areas, the solar contribution to the MIR, and the variation of surface emissivity between MIR and thermal IR, etc. (e.g. Giglio & Kendall, 2001; Giglio et al., 1999; Giglio & Justice, 2003; Shephard & Kennelly, 2003).

Due to the small size of the fire in comparison to the pixel, the potential impact from the 4 and 11 μm point-spread-functions (PSFs), including their coregistration, becomes a critical (and potentially the most important) source of error for a bi-spectral retrieval, regardless of satellite sensor. For example, Calle et al. (2009) showed that the fire pixel brightness temperature, for a given sub-pixel fire size and temperature, will greatly decrease when the sub-pixel fire is located near the edge of the pixel, and increase for fires near the pixel center. Additionally, the 4 and 11 μm PSFs may deviate near the pixel edge (misregistration), thereby increasing the potential error in retrieved fire area and temperature in these cases. Daytime solar reflection in the MIR channel can also have an impact on sub-pixel retrievals. Specifically, Li et al. (2001) showed that the contribution of reflected solar radiation in the AVHRR MIR channel increases as the surface temperature decreases. The solar contribution was also found to be highly dependent on the solar geometry and surface albedo. When considering the potential error sources (aside from coregistration), Giglio and Kendall (2001) found that the Dozier retrieval is possible when the fraction of the pixel encompassed by fire is greater than ~0.005 (0.003 for MODIS). Above this threshold, random retrieval errors will be within 50% and 100 K, at one standard deviation, for fire fractional area and temperature, respectively. However, uncertainties increase rapidly below the threshold.

Despite the potential for error, several advances have been made to sub-pixel retrievals over the past decade. One example is the Bi-Spectral Infrared Detection (BIRD) small satellite mission (operational from 2001–2004). The BIRD satellite had a pixel size of 185 m, saturation temperature of ~600 K, and MIR and TIR channels of 3.8 and 8.8 μm, respectively (Zhukov et al., 2006). In contrast to MODIS, the BIRD fire detection algorithm specifically included a component for a modified Dozier retrieval. To avoid the potential error sources, especially coregistration errors, the BIRD algorithm created pixel clusters using any adjacent hotspot pixels (Wooster et al., 2003; Zhukov et al., 2005, 2006). The modified Dozier retrieval was then performed on these clusters rather than individual pixels. Ground validation tests for controlled fires were performed (e.g. Oertel et al., 2004; Zhukov et al., 2005), but detailed assessments of wildfires, using higher resolution sensors, were not undertaken.

In recent years, a modified approach, using multiple endmember spectral mixture analysis (MESMA) to retrieve sub-pixel fire properties, has been developed (Dennison et al., 2006; Eckmann et al., 2008, 2009, 2010). MESMA assumes that the radiative signature of each pixel is a result of a linear combination of sub-pixel features (or endmembers), and thus the radiances at multiple channels can be used to disentangle the area fraction of each end-member (such as fire and non-fire) provided that the number of channels is larger than the number of sub-pixel features to be retrieved. The original method was used for classification of land surface type. In that case, a finite number of endmembers, each having unique land surface characteristics, was incorporated into the analysis. However, the application to wildfires is not straightforward because the number of fire classes can be infinite. Nevertheless, Eckmann et al. (2008, 2009, 2010) produced fire endmembers for a variety of temperatures over a variety of wavelengths. Therefore, the MESMA retrieval is essentially a Dozier retrieval over a variety of wavelengths instead of

two channels. Results from the MESMA and Dozier-type retrievals have been compared, but neither retrieval method could be shown to be superior with available validation data (Eckmann et al., 2009).

3.2. Developing a sub-pixel retrieval for MODIS

Since MODIS data became available from Terra in February of 2000, few attempts have been made to implement a MODIS sub-pixel retrieval, which is likely a result of the potential for error, especially from atmospheric effects (Giglio & Kendall, 2001). In this study, output from the Santa Barbara DISORT Atmospheric Radiative Transfer (SBDART) model is used to provide a representation of atmospheric effects prior to the calculation step, which avoids creating additional terms for atmospheric transmittance (as in Eqs. 5 and 6). SBDART considers many processes known to affect the ultraviolet through the infrared wavelengths allowing for detailed computations of plane-parallel radiative transfer within the Earth's atmosphere and at the surface (Ricchiazzi et al., 1998). Therefore, SBDART also includes the solar reflectivity term (I_{4ref}) in Eqs. (5) and (6). Based on previous studies, e_{4b} and e_{11b} are assumed to be respectively equal to 0.95 and 0.97 (e.g. (Giglio et al., 1999; Petitcolin & Vermote, 2002; Tang et al., 2009), which is true for relatively dense, green vegetation, such as the temperate evergreen forests used in this study. With this configuration and by including the MODIS spectral response function, SBDART is ready to incorporate all terms in Eqs. (5) and (6) to simulate the MODIS observation at its two fire detection channels (3.96 and 11.0 μm).

As a preliminary step, SBDART is run repeatedly for different combinations of the possible geometry values, background temperatures, and sub-pixel fire temperatures, and the output results are saved together with the input parameters as a lookup table at 4 and 11 μm. The input temperature values are the kinetic temperatures (not brightness temperatures) at the bottom of the atmosphere and range from the lower limits for a background temperature (277 K) to the upper limit for a sub-pixel fire (1500 K). Due to the location and time of the events used in this study (Fig. 1), the atmospheric profile is assumed to be a representative mid-latitude summer profile, which includes 2.9 g/cm^2 of water vapor in the atmospheric column. However, the sensitivity to variations in the atmospheric profile is examined in the second part of this study. The final SBDART output allows a lookup table, containing input surface temperature, solar zenith, viewing zenith, and relative azimuth angles, to be created as a function of top-of-atmosphere radiance. Once complete, these lookup tables are referenced repeatedly in the main retrieval process.

The actual retrieval, which is summarized in Fig. 2, implements the lookup tables to aid in solving Eqs. (5) and (6) for each MODIS fire pixel in any given MODIS scene (granule). However, the non-linear equations require the use of a multistep, iterative process to obtain fire area fraction and temperature. To begin, the observed MODIS geometries and the first input temperature are matched to the lookup table to obtain the top-of-atmosphere radiance of the pixel containing the fire. The algorithm then continues to cycle through all input temperatures (e.g. potential fire temperatures) and calculates the fire fraction using a variation of the method developed by Shephard and Kennelly (2003). A residual calculation is used to keep track of the fire temperature and area fraction corresponding to the best fit in the observed radiances for the 4 and 11 μm channels, and the final fire temperature and area fraction are selected based on the lowest residual.

Drawing from the BIRD satellite methodology, two clustering methods are implemented to alleviate random errors within the pixel-level retrievals. The first is a general summation method, where each individual pixel-level retrieved fire area is summed to obtain the area of an entire fire event. The second clustering method is a single retrieval (via averaging), which performs a single retrieval for all MODIS fire pixels corresponding to a given fire cluster. In this case, the sub-pixel calculations use the mean geometry values, mean pixel temperatures, and mean background temperatures of the fire pixel cluster. Following these pixel and cluster-level calculations, FRP_f is calculated via Eq. (2). Therefore, there are three major outputs from the retrieval at both the pixel and cluster-levels: fire area, fire temperature, and FRP_f. As mentioned in Section 3.1, specific sources of error can stem from indirect effects (e.g. PSF coregistration) to direct effects of background temperature, surface emissivity, and water vapor, etc. Section 6 of this paper examines the uncertainties from indirect error sources, while a detailed examination of sensitivity to direct error sources is left for the second part of this study.

4. MODIS and AMS data, their collocation, and pixel overlap corrections

MODIS sub-pixel fire information is retrieved from an integrated use of the following three data products, either from MODIS/Terra or MODIS/Aqua, at a spatial resolution of 1 km^2 at nadir: (1) level 1B radiance data (MOD021KM/MYD021KM), (2) geolocation data (MOD03/MYD03), and (3) level 2, collection 5 fire product data (MOD14/MYD14). Data sources (1) and (2) are used to provide the radiance of the entire pixel and all relevant geometry information, such as solar zenith (SZA), relative azimuth (RAZ) and viewing zenith (VZA) angles (e.g. Wolfe et al., 2002), while the fire product (3) provides information on fire locations, background temperature, and FRP_p. The sub-pixel retrieval is only applied to the pixels that are flagged as fire pixels by the standard MODIS fire product (3).

4.1. MODIS fire products: fire detection and FRP_p

MODIS is unparalleled in fire detection because of its ability to differentiate a wide range of fire intensities, as a result of the synergy between its two 4 μm (more precisely 3.96 μm) channels whose dynamic ranges are complementary (Justice et al., 2002). Fire pixels are retrieved using a hybrid, contextual process, which includes absolute and relative detection pathways. For absolute detection, a set of thresholds for reflectance at 0.86 μm and brightness temperature at the 4 μm and 11 μm infrared channels are used. The reflectance values of the 0.86 um channel are employed to reduce the “false-positive” effects of bright reflective surfaces and sun glint characteristics in a given scene that contains a mix of fire and those non-fire, highly reflective surface features. The brightness temperature thresholds at the 4 μm and 11 μm infrared channels are used to identify potential fire pixels (Giglio et al., 2003; Justice et al., 2002). The relative detection check is then incorporated to compare a pixel's spectral signature to surrounding background pixels. Finally, both checks are combined (as a Boolean union) to classify a potential pixel as a real fire pixel. The MODIS FRP_p (collection 5) is subsequently calculated for all fire pixels via Eq. (1). The higher saturation temperatures of MODIS allow for the derivation of FRP_p for nearly every fire it detects, because 1 km^2 pixels with $T_4 > 500$ K seldom occur in nature (Ichoku et al., 2008a).

The major caveats of the MODIS fire products are sun glint, coastal false alarms (water reflectance), and clouds that may hamper the fire detection. These non-idealities are accounted for by applying water masks and cloud masks in the fire detection algorithm (Giglio et al., 2003; Kaufman et al., 1998a). Using 30 m validation data (from ASTER and ETM+), Schroeder et al. (2008) show that the probability of detection approaches 80% when the number of 30 m fire pixels (contained within a MODIS fire pixel) approaches 75. The smallest detectable fire size in any given MODIS fire pixel was found to be ~100 m^2 (Giglio et al., 2003). Though hard to validate directly and globally, MODIS FRP_p was found to be in fair agreement with FRP_p measurements by other sensors in several sub-global spatial domains (Ichoku et al., 2008a; Roberts et al., 2005; Wooster et al., 2003). The FRP_p detection limits are about 9 and 11 MW for Terra and Aqua, respectively (Schroeder et al., 2010).

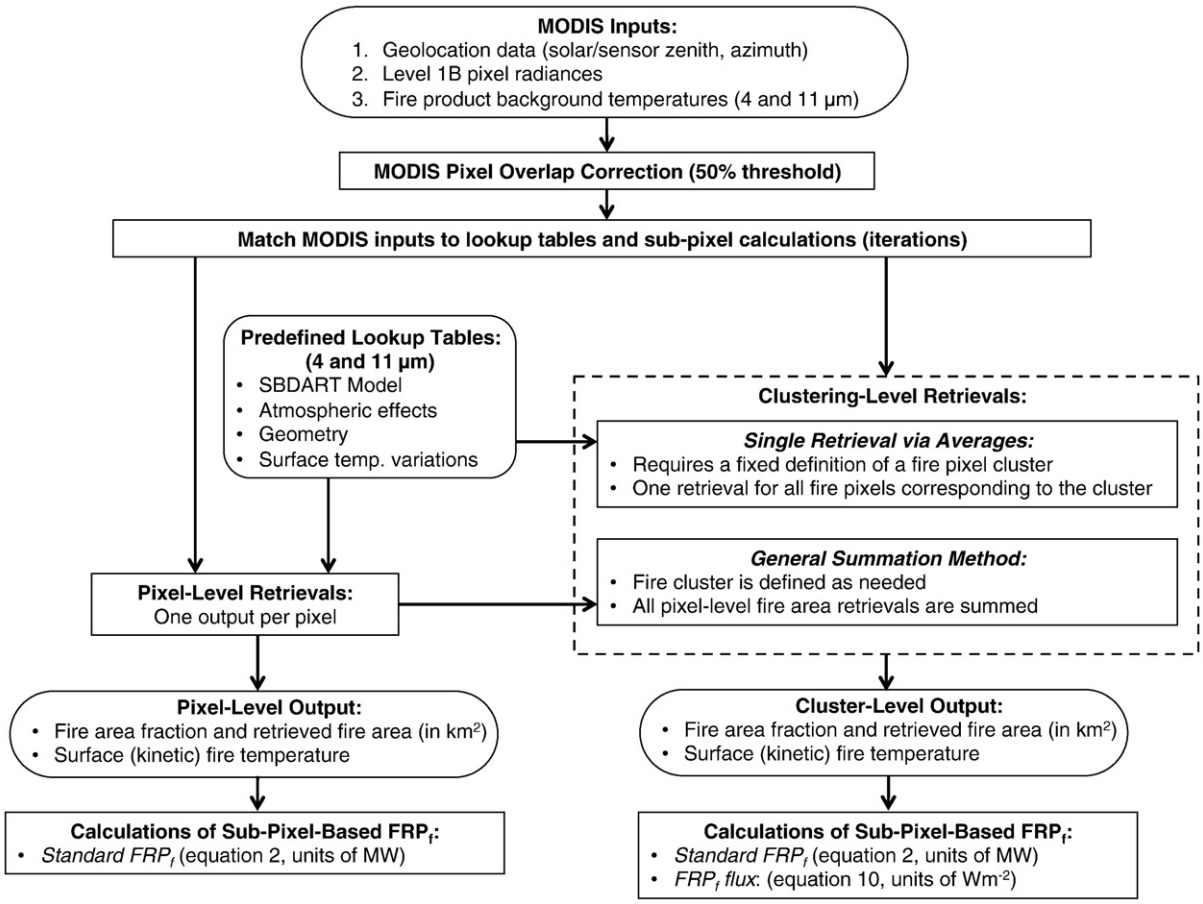

Fig. 2. Flowchart illustrating the MODIS sub-pixel retrieval and the subsequent calculation of FRP_f.

4.2. Autonomous Modular Sensor (AMS) observations

The AMS, flown aboard the NASA Ikhana Unmanned Airborne System (UAS) and additional piloted aircraft, provides the high-resolution data for the initial assessment of the MODIS sub-pixel retrieval. The AMS was put into operations in 2005 and offers pertinent spectral measurement capabilities, such as derivation of fire size, temperature, and serves as a potential airborne, higher spatial resolution FRP validation sensor. Both NASA and the United States Forest Service (USFS) have collaborated on the use of the AMS for supporting wildfire observations. The Ikhana UAS performance characteristics allow mission profiles that can extend from the Mexican border in the south to the Canadian border in the north and from the Pacific Ocean in the west to the Rocky Mountains in the east when operating out of its home base at NASA-Dryden Flight Research Center, Edwards, California (Ambrosia et al., 2011b; Ambrosia & Wegener, 2009). In addition, the Ikhana is capable of supporting day and night operations with a ~24 hour endurance, 150–200 knots airspeed, ~13,720 m (45,000 ft) altitude, and flight legs of over 7408 km (4000 nautical miles). A pilot located at a ground control station remotely controls the Ikhana. Piloted operations on various aircraft (Beechcraft B200 King-Air, etc.) have also been accomplished, though with shorter flight profile capabilities.

The AMS spatial resolution is controlled by the platform altitude and commonly falls in a range from 3 to 50 m. The total field of view (FOV) can be set at 43° or 86°, and the instantaneous field of view (IFOV) can be set at 1.25 mrad or 2.5 mrad (Ambrosia & Wegener, 2009). Both the FOV and IFOV are user selectable based on the mission requirements. For example, an altitude of 7011 m (23,000 ft) Above Ground Level (AGL), with a 2.5 mrad IFOV would provide a spatial resolution of 15 m (Ambrosia & Wegener, 2009). The AMS is a multispectral instrument with 12 spectral channels in the visible through thermal-infrared (Ambrosia et al., 2011a, 2011b). Fire hot spots are detected near 4 and 11 μm using AMS channel 11 (3.75 μm) and channel 12 (10.76 μm) (Ambrosia et al., 2011b; Ambrosia & Wegener, 2009). Originally applied to AVHRR imagery (Li et al., 2000b), the AMS fire detection algorithm is based on that developed by the Canadian Center for Remote Sensing (CCRS) and provides general hot spot information for each AMS scan (Cahoon et al., 1992; Flasse & Ceccato, 1996; Li et al., 2000a, 2000b, 2001).

In this study, a separate AMS fire detection algorithm, developed specifically for an initial assessment, is used to identify the individual flaming regions within a given MODIS fire pixel (see Section 5). This new algorithm is based on the unique challenges encountered when applying the AMS to obtain the precise area of a sub-pixel fire. For example, changes in flight altitude and surface topography can affect the AMS background temperature and fire detection thresholds within a scan or from scan-to-scan. Therefore, in the initial assessment algorithm, each threshold is image-based and allowed to vary within the boundaries of each MODIS fire pixel. The AMS data collected in 2007 are saturated in the 4 μm channel, with saturation temperatures varying from 510 to 530 K, depending on the flight characteristics. At spatial resolutions of 50 m or better, this saturation level means that many fire pixels are saturated, which precludes fire temperature or FRP investigations using these data. Approximations of fire temperature can also be achieved using the unsaturated 11 μm channel, but limitations are introduced due to the lower sensitivity at higher temperatures. The AMS engineering team is currently exploring modifications to the scanner, which would allow a large increase in the measured pixel temperatures of the ~4 μm channel, thereby facilitating an increased probability of accurately determining fire pixel FRP estimates.

4.3. AMS and MODIS collocation

Several AMS flight data scans, from August to October 2007, were available for this study, which include single fires and multiple fire events on the data collection dates. The high spatial resolution (~15 m) AMS data, collected near-coincident with MODIS acquisitions, allow for a determination of the fire hot spots within the MODIS fire pixels corresponding to a given fire event (Fig. 3). With a wide range in topography and biomass type (Westerling et al., 2003), the western United States is known to experience a wide variety of burning conditions. These variables affect the fire rate of spread, which can reach 34 meters per minute (~0.5 km per 15 minutes) in the chaparral of Northern California (Stephens et al., 2008), suggesting that some fires may change drastically in a short time period. The large Zaca Fire example in Fig. 3 has a time lag of approximately an hour between the MODIS overpass and the AMS flight, which explains some fire location dissimilarities between the MODIS and AMS detections. Therefore, to produce an accurate assessment, the temporal difference between AMS and MODIS was limited to a maximum of 15–17 min before or after the MODIS overpass, ensuring that MODIS and AMS are observing the same fire characteristics, near-simultaneously.

After applying the temporal limitation, a total of six collocated cases (displayed in Fig. 1) are available from the 2007 dataset, which include day, night, nadir, and off-nadir MODIS observations. Specifically, four MODIS scenes (granules) are used to provide the six collocations. Of these, cases #1–4 are from a single Santa Ana burning event in Southern California (24–28 October 2007) and cases #5 and #6 are from a fire event in Northern California on 9 September 2007. The Ikhana commonly flies over the same fire event multiple times on adjacent flight tracks, used to derive a "mosaic" of the total fire event region. The AMS on the Ikhana has also been used to capture the same fire event during two (or more) time periods in a day to derive fire progression and some AMS fire data scans can be as short as 3 min. Therefore, by examining neighboring, short duration AMS scans, it is possible for a single MODIS scene to provide more than one collocation (e.g. cases #5 and #6 in Fig. 1). A spatial investigation is conducted to minimize any overlapping MODIS fire pixels between collocation cases. Even still, three fire pixels overlap between cases #3 and #4 and one fire pixel overlaps cases #5 and #6. The specific details for calculating MODIS pixel dimensions are provided in following section.

4.4. Calculating pixel area and accounting for MODIS pixel overlap

Another MODIS characteristic affecting sub-pixel retrieval is the potential for off-nadir fire detection errors (e.g. Giglio & Kendall, 2001). The "bowtie" scanning method of MODIS results in pixel overlap near the edge of the granule (e.g. Gomez-Landesa et al., 2004; Masuoka et al., 1998), which can result in the same fire being counted in more than one scan, effectively producing duplicated – though not identical – fire pixels. Therefore, to retrieve accurate fire size, any pixel overlap must first be removed (shown in Fig. 2), especially for the clustering analysis step. To begin, the pixel corners are calculated by averaging the four pixel centroid points (provided by MODIS) surrounding each corner. This calculation is different than the MODIS pixel size approximation provided by Giglio (2010), which provides a standardized calculation for every MODIS scene based on the pixel's VZA and recognizes that MODIS pixels realistically have soft, non-rectangular edges. However, this study requires an approximation of the specific boundaries of each pixel to account for any potential variations in pixel size caused by variations in local topography and to facilitate the collocation of the AMS data. As a result, the dimensions of each MODIS pixel are calculated on a scan-by-scan basis and steps are taken to minimize any error at the scan edges. With this information, the area of each MODIS pixel is subsequently calculated, allowing the true area of a fire (in km^2) to be calculated from each retrieved fire fraction (Section 3.2). In general, the calculated pixel areas fall within 5–12% of the values obtained via the Giglio (2010) approximation.

The actual overlap correction takes advantage of the similarities within every MODIS granule. For example, every granule contains 204 scans composed of 10 scan lines along-track (Wolfe et al., 2002), each with an along-scan width of 1354 pixels (one scan = 10 × 1354 pixels or about 10 × 2300 km). While the average pixel size near-nadir is 1 km^2, off-nadir pixel growth causes the total scan width to grow to 2300 km rather than 1354 km. Based on these similarities, any pixel that overlaps another pixel in one granule will overlap that same pixel in every granule. Therefore, by assuming the Earth is a perfect sphere and topographic influences are minimal, a general overlap correction can be developed and applied to all MODIS granules. For this study, a pixel is defined as an overlapping pixel if it overlaps a pixel in the previous scan by 50% of its total area. This overlap definition is then tested on every pixel on a scan-by-scan basis. For example, the locations and dimensions of each individual pixel within the second scan are

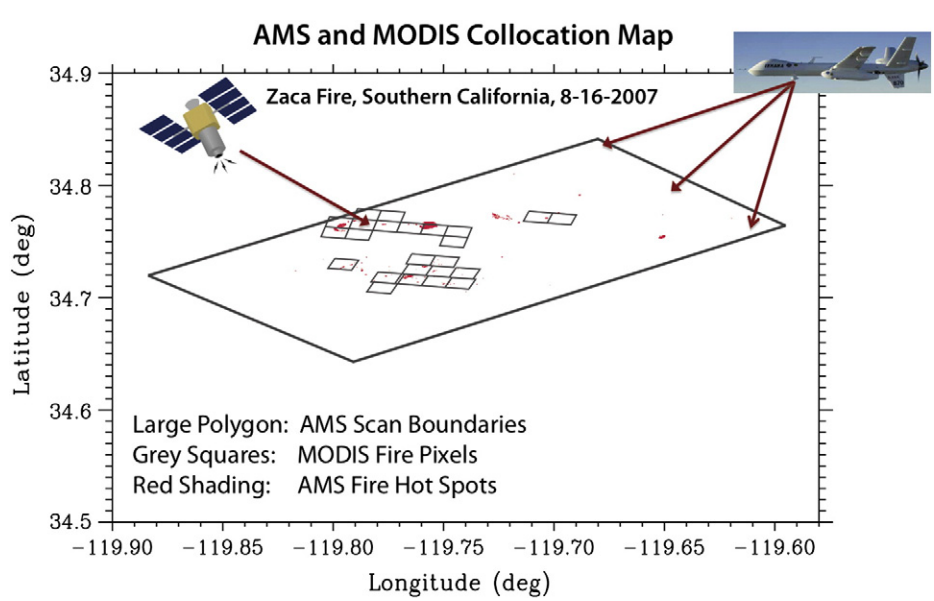

Fig. 3. Example AMS and MODIS collocation map for the large Zaca Fire in August 2007. There is approximately an hour time lag between the MODIS overpass and the AMS flight.

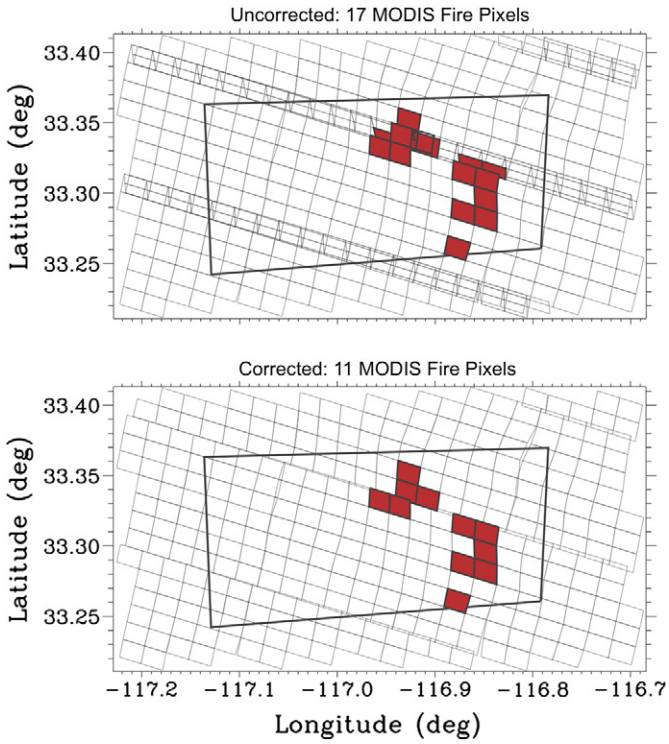

Fig. 4. An example MODIS and AMS collocation case (case #4) at a MODIS viewing zenith angle of 50.3°. (Top) Without a pixel overlap correction and (Bottom) with a pixel overlap correction. Black polygons denote the boundaries of the AMS scan and the pixels shaded in red are the MODIS fire pixels contained within the AMS scan.

compared to the first scan's pixel locations and dimensions. The algorithm keeps track of the locations (index) of any pixels that overlap the first scan and the process repeats for each subsequent scan in the granule. The end result is an index of pixel locations that must be removed from each scan in any MODIS granule.

While pixel overlap may allow for multiple vantage points of the same fire at the individual pixel level, future applications will not have high resolution data available to discern which of these vantage points is the best, and any overlap will also influence the cluster-level results. Therefore, an overlap correction is used in each collocation case to reduce the chance of artificially large fire clusters, which is especially critical for the general summation clustering method (described in Section 3.2). Even with the overlap correction, small instances of overlap and small gaps may still exist, but the pixel grid will become much more realistic, especially at larger VZAs. As an example, the overlap correction was tested on one of the six collocation cases (case #4) with a mean VZA of 50° (Fig. 4). Without a correction, this case had a total of 17 MODIS fire pixels and displayed considerable pixel overlap. However, when applying the correction to select only the non-overlapping pixels, the pixel grid clears up and the total number of fire pixels is reduced to 11. The specific details for each collocation case are presented in Table 1 and show that the overlap correction does little to alter the pixel grid when the VZA is less than ~35° (near-nadir), but the number of fire pixels can decrease by more than 50% at large VZAs after the correction is applied.

5. AMS fire detection algorithm and background temperature

Similar to MODIS, AMS fire detection requires the use of thresholds, which can be somewhat subjective (Giglio et al., 2003; Justice et al., 2002; Kaufman et al., 1998a). Due to the shift in the peak of the Planck Function toward shorter wavelengths at high temperatures, fire

Table 1
Specifics of the case studies and results of the pixel overlap correction.

Collocation Case #	Date	Overpass Day/Night	Mean Viewing Zenith Angle	# Fire Pixels Uncorrected	# Fire Pixels Corrected
1	10–28–2007	Day	13	7	7
2	10–26–2007	Day	32	5	5
3	10–24–2007	Day	50	10	9
4	10–24–2007	Day	50	17	11
5	09–08–2007	Night	64	7	3
6	09–08–2007	Night	64	4	2

detection thresholds are typically based on the 4 μm channel. However, detection algorithms for different sensors, such as MODIS and GOES, consider the 11 μm channel to varying degrees (Giglio et al., 2003; Prins & Menzel, 1994). For example, MODIS incorporates the temperature difference between 4 and 11 μm and the early GOES algorithm set a specific fire detection threshold for the 11 μm channel. In the case of AMS, an 11 μm fire threshold is used as a secondary check when saturation is reached at 4 μm. Through an automated process, the AMS fire detection thresholds are allowed to vary for each MODIS pixel and adapt to the unique characteristics of the AMS instrument. The AMS algorithm is not meant for operational purposes and is specifically designed to process the AMS data points contained within a single MODIS pixel.

Within any MODIS pixel, there are between 4000 and 9000 AMS data points depending on the location relative to the AMS nadir and the flight altitude (Fig. 5). These data points allow for a detailed investigation of the 'mixed' MODIS fire pixels, which commonly contain a background, smoldering, and actively burning region (e.g. Eckmann et al., 2008; Kaufman et al., 1998a). However, it is assumed that the temperature difference between actively burning and smoldering regions is larger than the difference between background and smoldering. Hence, AMS fire detection is currently aimed at obtaining the mean state of temperature and fire size of two groups: (1) the data points of actively burning fires, and (2) the data points of the remaining region (including smoldering and cooling). The smoldering region is largely neglected because the collocated cases (#1–6) are very intense fire events and the sub-pixel calculation is likely weighted toward retrieving the flaming region (largest contribution to pixel MIR radiance). Fire modeling studies have shown that the depth of a fire front commonly ranges from a few meters to ~30 m for grassland fires (Mell et al., 2007) and can reach 400 m in dense vegetation (Filippi et al., 2009). Based on the potential fire front size, it is expected that the AMS fire area fractions, within a MODIS pixel, will typically fall below ~0.2.

5.1. Background temperature and minimum thresholds

The AMS fire detection process is based on the histogram at 4 and 11 μm and begins with background temperature selection. In contrast to the neighboring pixel method for MODIS background temperature (Kaufman et al., 1998a), the histogram method for background temperature considers the temperature of the unburned AMS data points within the MODIS fire pixel (in-pixel background temperature). This method is necessary because the AMS flying altitudes vary case by case, and hence any thresholds on temperature should be image based. Due to the scanning method of AMS, topographic effects, and aspect, the cool region of the pixel can vary 5–10 K (Fig. 6). However, this variation is not likely over a 1 km distance unless there is a rapid change in elevation. Therefore, to account for any of these observational differences, the AMS background temperature calculation at 4 and 11 μm (dash-dotted blue lines in Fig. 6c,d) is a weighted average of all

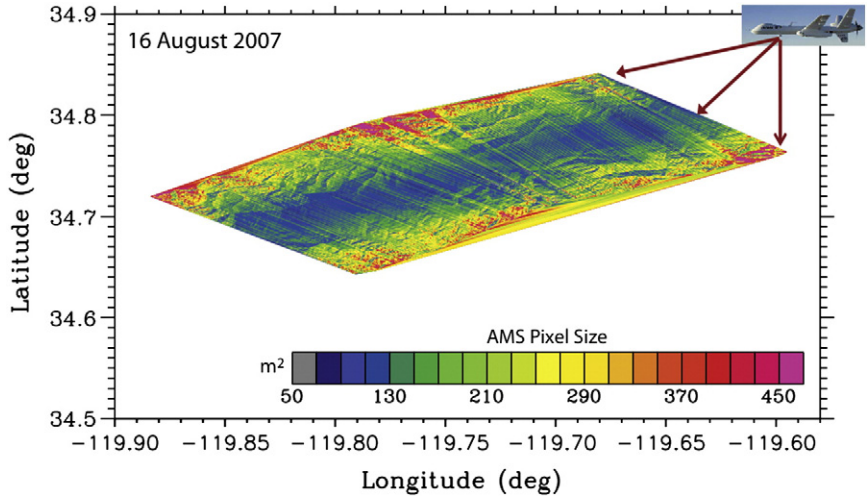

Fig. 5. Visualization of the variation in AMS pixel size (resolution in m^2) based on the location within the scan and elevation. Cool colors indicate regions of higher resolution and warm colors indicate the coarsest resolution.

temperature bins (in the histogram) less than the median. A visual inspection of each histogram is also undertaken to be certain that the calculated AMS background temperatures are representative of only the non-burning portion of the pixel. The AMS background temperature can then be compared to the MODIS background temperature (green dashed lines in Fig. 6c,d).

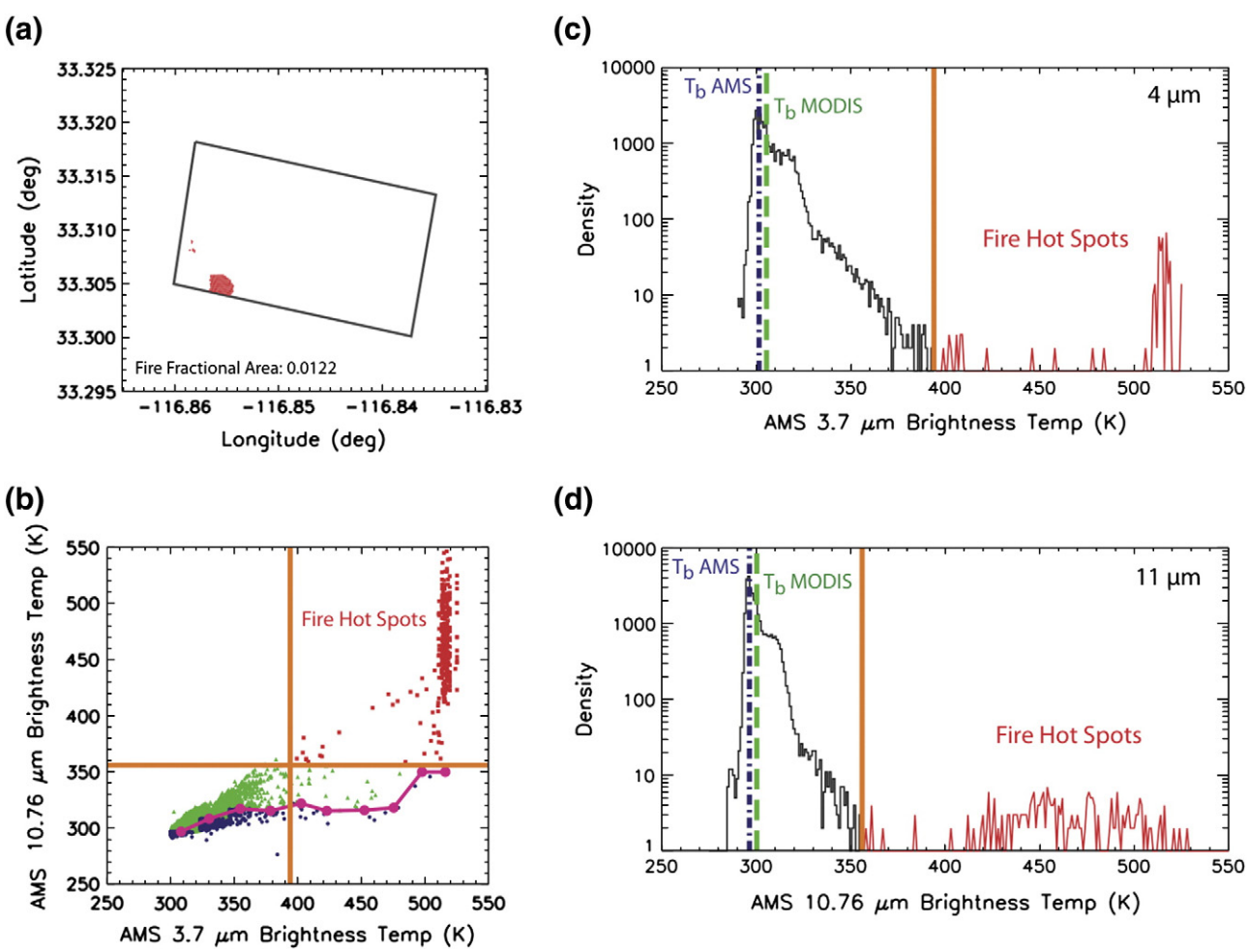

Fig. 6. Example of AMS daytime fire detection within a MODIS pixel. (a) Map containing the AMS hot spot detections within a MODIS pixel. (b) Scatterplot of AMS 4 and 11 μm brightness temperatures. Blue dots indicate AMS data points disregarded as fires, green triangles indicate the region to be examined as potential fires, and red squares indicate the final AMS fire detection. Fire detection thresholds are displayed as solid orange lines and the minimum threshold is displayed as a solid pink line, with each dot corresponding to the center of an ICT test bin. (c) and (d) Histograms used in AMS fire detection at 4 μm and 11 μm, respectively. Fire detection thresholds are displayed as solid orange lines, and the MODIS and AMS background temperatures are respectively displayed as dashed green and dash-dotted blue lines.

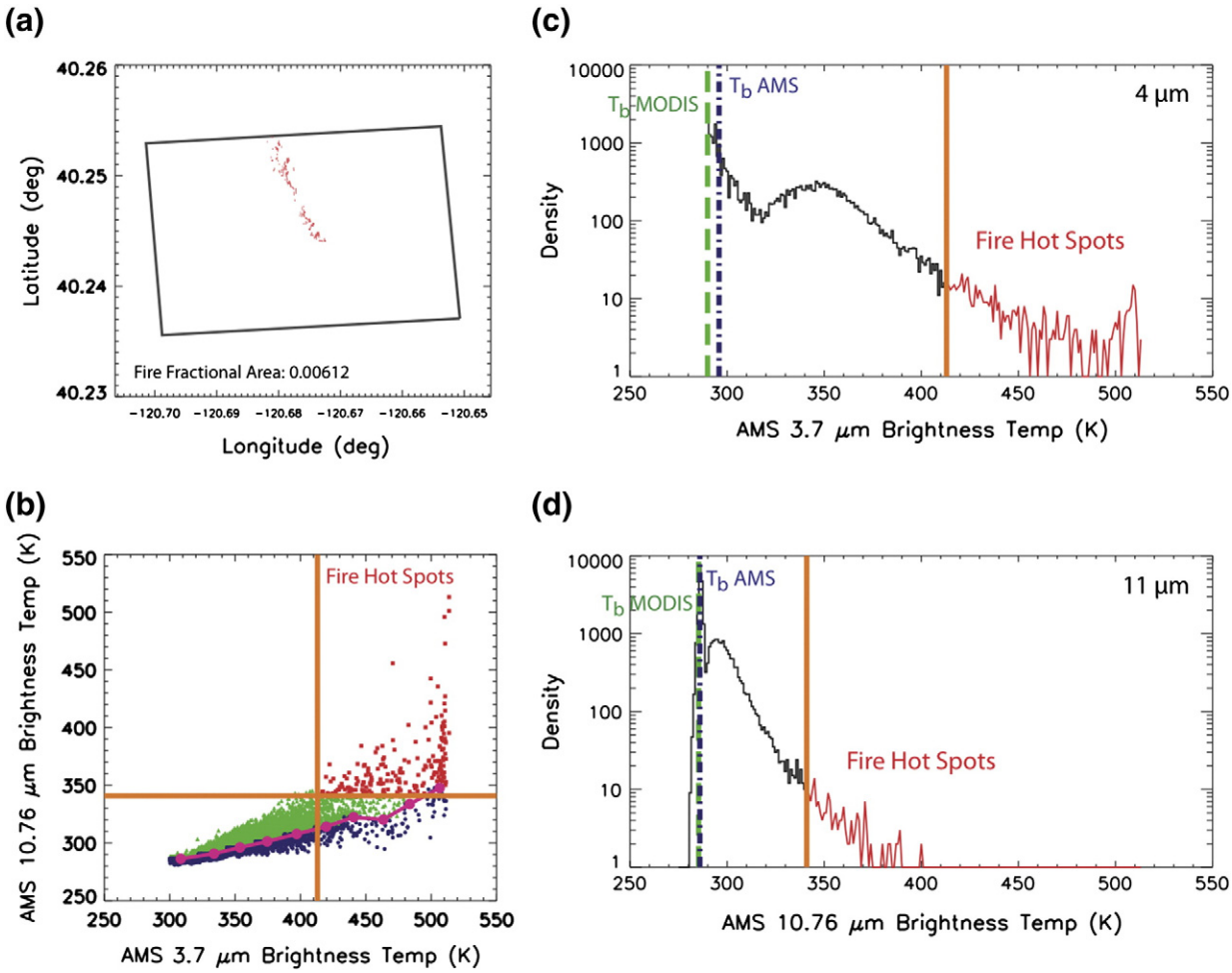

Fig. 7. Same as Fig. 6, but for AMS nighttime fire detection within a MODIS pixel.

Following the background calculations, any AMS data points that are obviously not fire hot spots (blue dots in Fig. 6b) are removed using an interchannel comparison test (ICT), which searches for any AMS data points that are cooler than the background temperature or display cold 11 μm temperatures at high 4 μm temperatures. The ICT is necessary because of variability in the AMS data from scan to scan that results from varying saturation levels, flight altitudes, and scan widths. Specifically, the ICT calculation divides the range of the 4 μm temperature (~290–525 K) into ~10 bins and computes the 25% quartile of the 11 μm temperature within each 4 μm bin. Any temperatures that are less than the 11 μm 25% quartile are disregarded as potential fires (pink line in Fig. 6b). However, if the 25% quartile is above 350 K, then the ICT threshold is set to 350 K. Any AMS data points above the resulting ICT minimum threshold line move on to be considered as fire hot spots (green triangles in Fig. 6b).

5.2. Daytime and nighttime fire detection thresholds

The actual AMS fire detection thresholds (day and night) are calculated for both the 4 and 11 μm channels (orange lines in Fig. 6) using the temperature histograms of each channel. During the day, considerable variability is added to the histograms from uneven surface heating and solar effects, making it difficult to separate the data points of the actively burning region. Even with this daytime noise, it is assumed that actively burning portions of a MODIS pixel will show some separation from the cooler portions in the histogram. Therefore, several bins with a low density in the 4 or 11 μm histograms are the starting point for the fire detection thresholds. At 11 μm, the histogram is searched, starting from the minimum threshold, for the first region with at least 5 bins displaying a density less than two. The fire threshold is then set to the lowest value within the region of low density.

The fire threshold method at 4 μm is slightly different due to saturation occurring between 510 and 530 K. It is assumed that any AMS pixel at the saturation level is hot enough to be considered. However, the remaining data between the ICT minimum threshold and the saturation level must also be investigated. The procedure begins by calculating the high temperature median (HTM), defined as the median of all AMS data points above the ICT minimum threshold. All AMS data points below the HTM are subsequently searched for a region of low density as in the 11 μm procedure. However, in this case, the region of low density is defined as a region with at least 4 bins displaying a density less than one. The limits are stricter than for 11 μm because the region under consideration is at relatively low temperatures and in many cases, the fire threshold will not exist below the HTM. In addition, the 4 μm data displays more variability at higher temperatures than 11 μm, which requires stricter limitations. As with 11 μm, the fire threshold is then set at the bin with the lowest value within the region of low density. If a region of low density is not found below the HTM, then the HTM itself is used as the 4 μm fire threshold.

The region of low density definition is very strict because the emphasis is on retrieving the actively burning region. If the density thresholds are increased, the retrieved fire area will be larger. However,

increasing the density threshold by one at 4 and 11 μm will only produce a relative increase in fire area of approximately 10%. In contrast, increasing the density thresholds by three will increase the retrieved fire area by 40%. In this case, the 11 μm (4 μm) region of low density would be defined as the first region with at least 5 bins displaying a density less than five (four). Obviously, a much larger region of the histogram would then be considered as fire. Therefore, the region of low density is based on the area of minimum sensitivity.

The nighttime fire thresholds are more straightforward than the daytime thresholds. Reduced background noise allows for a detection approach similar to MODIS, where separation is obtained by selecting pixels with temperatures that are a few standard deviations from the mean (Giglio et al., 2003; Justice et al., 2002). Specifically for AMS, the fire thresholds at 4 and 11 μm are set at two standard deviations from the mean (Fig. 7). Regardless of daytime or nighttime, the 4 and 11 μm fire thresholds are not allowed to fall below 380 K and 340 K, respectively. These minimum values are rarely reached, but are necessary for MODIS pixels containing only a few hot AMS data points (very small fire fractions). Any AMS data points with a temperature greater than the 4 and 11 μm fire thresholds are flagged as fire hot spots (red squares in Figs. 6b and 7b). The area of these AMS pixels is then summed to calculate the fire hot spot area within the MODIS pixel under consideration (assessment data, displayed in Figs. 6a and 7a). In some cases, negative radiance values will occur adjacent to a region of hot, saturated AMS

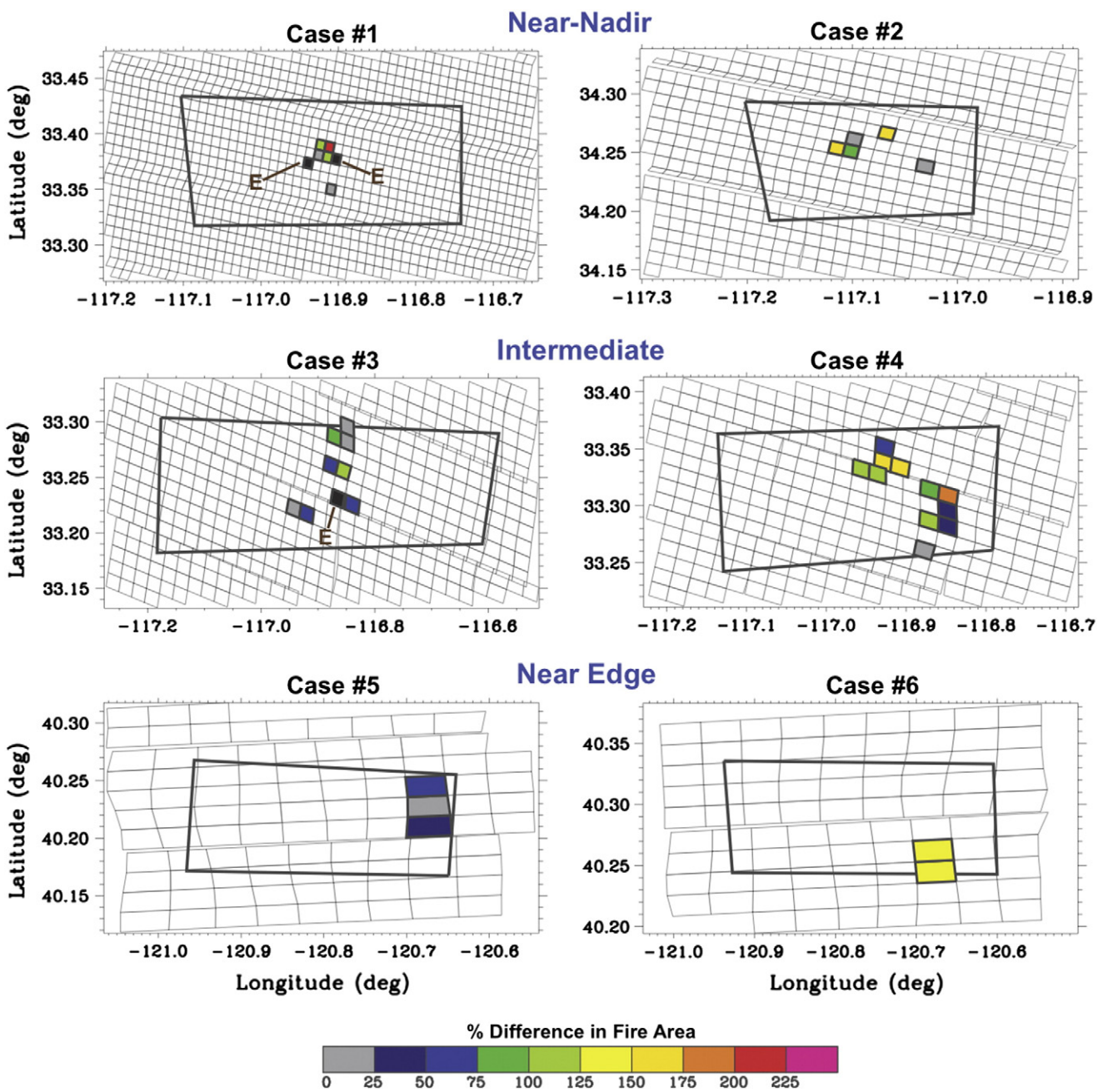

Fig. 8. Spatial representation of all six case studies in California. The large black polygons denote the boundaries of the AMS scan and smaller gray polygons represent the MODIS pixel mesh (corrected for overlap). The MODIS fire pixels are shaded in color based on the percent difference between the AMS observed and the MODIS retrieved fire area. The three pixels shaded in black and corresponding to a brown "E" indicate where the MODIS background temperature was higher than the fire pixel temperature (retrieval error). The viewing zenith angle increases from case #1 (13°) to case #5 and #6 (64°).

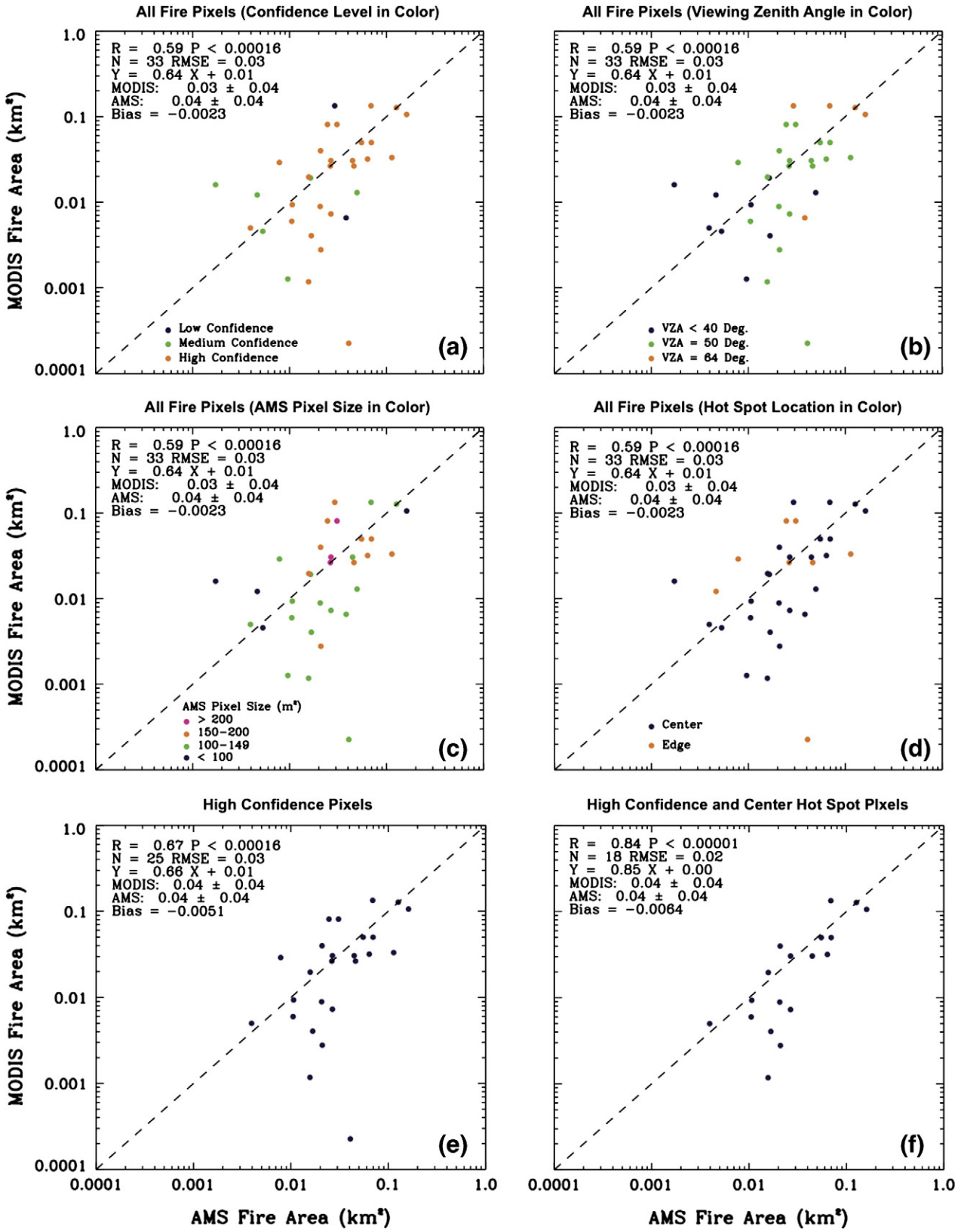

Fig. 9. Pixel-level comparisons between retrieved MODIS fire area and AMS observed fire area from all six collocated cases. (a) Color scheme indicates the fire detection confidence level provided by the MODIS fire product. (b) Color scheme indicates the viewing zenith angle (distance from nadir). (c) Color scheme indicates the variation in AMS pixel size (based on Fig. 5). (d) Color scheme separates the pixels with distinct sub-pixel hot spots located on the pixel edge from the remaining pixels. The statistics corresponding to the color schemes in (a–d) are presented in Table 2. The idealized cases, which contain only the high confidence and the combination high confidence/center hot spot fire pixels, are displayed in (e) and (f), respectively. For display purposes, (a–f) use a log vs. log scale. However, the statistics reflect the linear regression.

pixels. However, negative AMS radiance values usually comprise a very small faction of the total number of AMS pixels within a MODIS fire pixel footprint, and are currently disregarded.

6. Comparing the MODIS retrieved fire area with AMS observations

The ~15 meter resolution AMS fire data provide a direct ground assessment (in km^2) for the retrieved fire areas within each MODIS fire pixel. From a spatial perspective, Fig. 8 shows that 12 of the 37 MODIS fire pixels have retrieved fire areas within 50% of the AMS value, while the fire area for 3 of the MODIS pixels cannot be retrieved due to background temperature mischaracterization. These 3 pixels have an 11 μm background temperature that is warmer than the fire pixel temperature, which stems from the current MODIS fire detection algorithm and may be caused by heterogeneities (noise) in the region of background pixels (e.g. Kaufman et al., 1998a; Zhukov et al., 2006). Interestingly, there is a MODIS fire pixel in case #1 that does not contain any AMS fire hot spot detections, and is therefore the largest error displayed in Fig. 8. This pixel was not flagged as high confidence by the MODIS fire detection algorithm and may be a MODIS false detection (described in the following section). The remaining 21 valid fire pixels display significant deviations in retrieved fire areas from the counterparts of the AMS observations, which is expected based on the large potential for pixel-level errors highlighted in earlier studies (e.g. Giglio & Kendall, 2001). Therefore, the following sections focus on the analysis of several indirect, random processes than can partially explain the large differences between the MODIS and AMS pixel-level fire areas.

6.1. Specifics of pixel-level comparisons

For all MODIS fire pixels, AMS and MODIS fire area comparisons (Fig. 9a-d) have shown promise for a fire area greater than ~0.001 km^2 (1000 m^2), which corresponds to a fire area fraction of 0.001 in a 1 km^2 MODIS pixel. While the overall bias is low, pixel-by-pixel differences in AMS-MODIS fire areas are significant, producing a modest correlation (R = 0.59). It is also interesting that all 33 fire pixels displayed in Fig. 9a-d have an AMS observed fire area greater than 0.001 km^2 (1000 m^2), which is above the lower limit of MODIS fire detection for a reasonable retrieval accuracy (Giglio et al., 2003). Even though few fire pixels have an AMS fire area between 0.0001 km^2 and 0.003 km^2, a range that is expected to have the greatest potential for error in the retrieval, it is still generally observed that the relative variation in retrieved fire area is smaller for larger fires (>0.015 km^2) and larger for AMS fire areas below 0.01 km^2.

The MODIS fire product provides detection confidence levels for each fire pixel (Giglio, 2010), which can be investigated in the context of the sub-pixel results (Fig. 9a, Table 2). For example, the majority of fire pixels in the six case studies are flagged as high confidence with only eight pixels flagged as medium or low confidence. AMS observations show that the high confidence pixels contain the largest mean fire area (0.043 km^2). In contrast, the medium confidence pixels have a much smaller mean fire area (0.015 km^2), which is expected because the smaller sub-pixel fire area likely produces a fairly small increase in mean pixel brightness temperature. Therefore, the current MODIS algorithm may reduce the confidence level for these pixels. The two low confidence pixels actually have a larger mean fire area, but the bias is very large (105.88%). In contrast, the bias is greatly reduced with the high confidence pixels (−11.62%), suggesting that the results from higher confidence pixels show stronger agreement with the AMS observations (Table 2). This observation suggests that the MODIS low and medium confidence levels generally represent the small fires or the outliers in the retrieved sub-pixel areas, at least for the pixels used in this study.

Surprisingly, the location relative to nadir has a minimal effect on the retrieved fire area bias (Table 2), but pixels with larger VZAs have a large mean retrieved fire area of 0.102 km^2, while the pixels with small VZAs have a lower mean retrieved fire area of 0.009 km^2. This observation is expected because the MODIS pixel size increases dramatically with large VZAs, resulting in an increase in the smallest detectable (and retrievable) fire area (Giglio, 2010). However, all cases, regardless of pixel location, display considerable variability at the pixel-level with some retrieved fire areas matching the AMS observations and other pixels deviating from AMS by an order of magnitude or more (Fig. 9b). Therefore, it is likely, and will be shown below, that other indirect factors, such as the size and location of the fire within the pixel, have the greatest impact on the retrieval results. The potential impacts from variations in AMS pixel geometry (as displayed in Fig. 5) are considered in Fig. 9c, but this does not seem to have a major impact on the assessment results.

Drawing from earlier studies (e.g. Calle et al., 2009), the impacts from the 4 and 11 μm PSFs must be investigated examining the sub-pixel physical disposition of fire. For example, sub-pixel fire hot spots near the edge of a pixel will likely result in an underestimated fire pixel brightness temperature, while fires near center of a pixel may overestimate the pixel's brightness temperature. Similarly, a fire located on the boundary between pixels, will likely increase the brightness temperature of both pixels. This may help to explain the probable MODIS false detection in case #1 because the pixel boundaries (on two sides) are located near the sub-pixel fire hot spots contained within the adjacent pixels. A closer examination of the AMS fire data, displayed in Fig. 10, indicates that there are three major distributions of fire hot spots within the MODIS fire pixels used in this study: (1) center hot spot pixels, (2) edge hot spot pixels, and (3) a long fire front, which bisects the pixel. By using similar visualization methods, it was discovered that 8 of the 33 MODIS fire pixels contain pixel-edge fire hot spots (Fig. 9d). The center and edge hot spot pixel samples have nearly identical mean observed and retrieved fire areas with a very low bias (Table 2), but 6 of the 8 edge cases show significant deviations in retrieved fire area from the AMS observations and the pixel with the largest error in retrieved fire area is an edge case. The low bias in Table 2 results from similar magnitudes of overestimated and underestimated retrieved fire areas for the 8 pixels containing edge hot spots. In the non-edge hot spot cases, especially those with distinct center hot spots (e.g. Fig. 10a), it is possible that error may be introduced from a pixel brightness temperature that is overestimated (a potential bias). However, the edge cases are more likely to suffer from inter-channel,

Table 2
Statistics corresponding to the color scheme used in Fig. 9a–d.[a]

Variable (Indirect Effect)	# Pixels Out of 33	Mean AMS Fire Area km^2	Mean MODIS Fire Area km^2	Bias km^2	Bias %
MODIS confidence level (Fig. 9a)					
Low	2	0.034	0.070	0.036	105.88
Medium	6	0.015	0.011	−0.004	−26.67
High	25	0.043	0.038	−0.005	−11.62
Viewing Zenith angle (Fig. 9b)					
VZA<40°	9	0.013	0.009	−0.004	−30.77
VZA = 50°	19	0.035	0.029	−0.007	−20.00
VZA = 64°	5	0.085	0.102	0.017	20.00
AMS pixel size (Fig. 9c)					
>200 m^2	3	0.028	0.046	0.018	64.29
150–200 m^2	10	0.046	0.047	0.001	2.17
100–149 m^2	16	0.032	0.025	−0.007	−21.88
<100 m^2	4	0.043	0.035	−0.009	−20.93
Location of sub-pixel hot spots (Fig. 9d)					
Center	25	0.037	0.034	−0.003	−8.11
Edge	8	0.037	0.036	−0.001	−2.70

[a] Negative bias indicates that the mean AMS fire area is greater than the mean MODIS retrieved fire area.

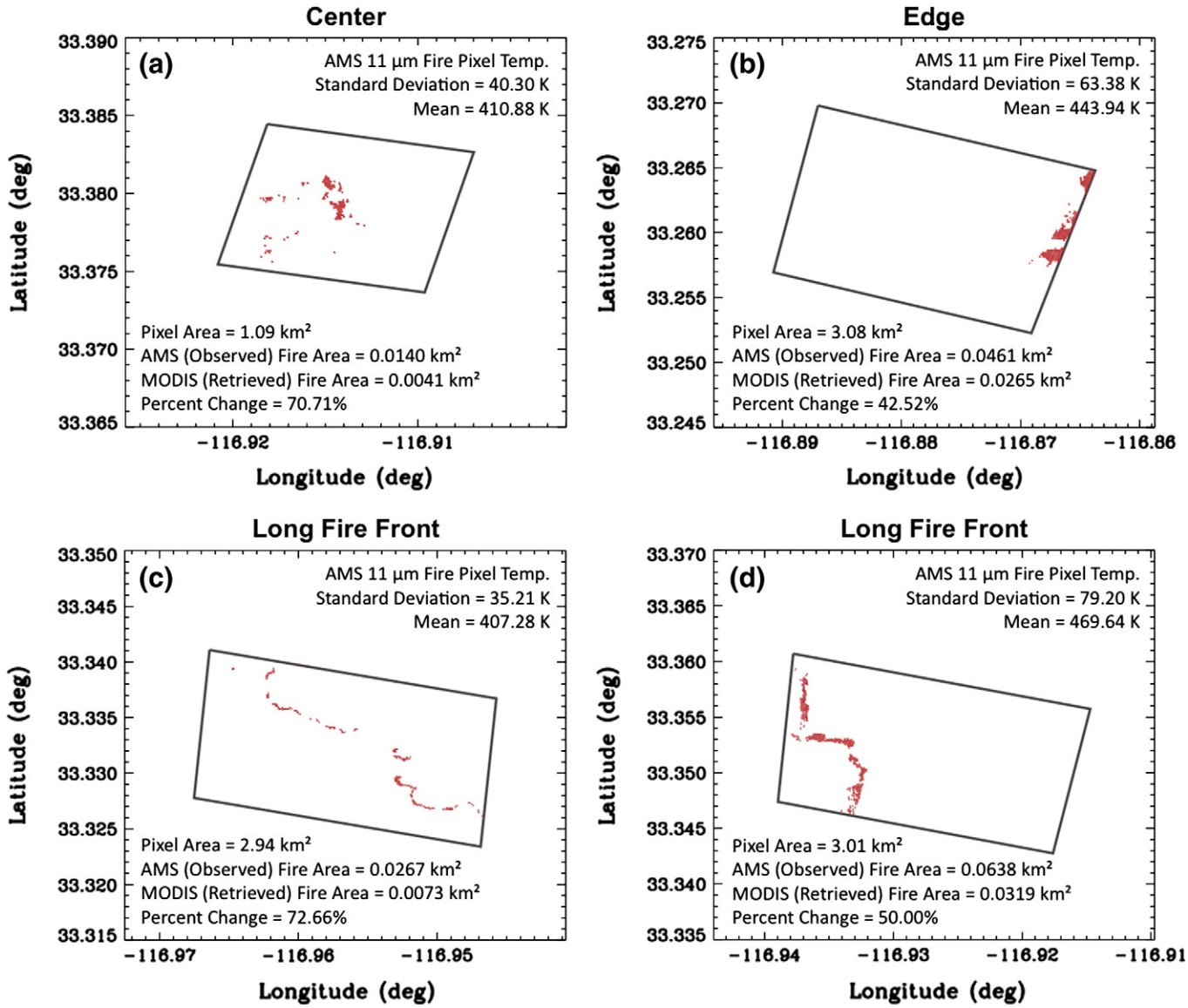

Fig. 10. Spatial display of the sub-pixel fire region within four MODIS fire pixels showing (a) center hot spots, (b) edge hot spots, and (c), (d) long fire front situations. Black polygons indicate the boundaries of the MODIS fire pixels and red shading indicates the locations of fire hot spots as observed by the AMS.

PSF coregistration errors (Calle et al., 2009; Shephard & Kennelly, 2003), and are therefore more likely to increase the potential for error in the sub-pixel retrieval output.

Along with PSF effects, the combination of sub-pixel fire size, temperature, and the overall distribution of sub-pixel hot spots can affect the retrieved fire area. For example, Fig. 10a,b shows a somewhat counterintuitive result where the center hot spot case has a larger error in retrieved fire area (70.71%) than the edge hot spot case (42.52%). The 11 μm AMS channel, though limited by reduced sensitivity at high temperatures, shows that the edge case has a much higher mean fire temperature (443.94 K) than the center case (410.88 K) and both cases are very heterogeneous (large standard deviation). Hot spots occupy about the same fractional area of each pixel (~0.01 for the 1 and 3 km^2 pixels), but the edge hot spot case contains an organized, large cluster of hot spots and the center hot spot case contains a more diffuse hot spot cluster spread over a large portion of the pixel. Therefore, it is possible that the pixel brightness temperature of the edge hot spot case is more representative of the observed sub-pixel fire properties than the center hot spot case, even when considering PSF effects. Similarly, the fire front case in Fig. 10c has a larger error in retrieved fire area (72.66%) than Fig. 10d (50.00%), but, unlike Fig. 10a,b, the fire fronts in Fig. 10c,d do not occupy the same area fraction of the ~3 km^2 pixels. Fig. 10c contains a small and very narrow fire front with a low 11 μm mean fire temperature (407.28 K), while the fire front in Fig. 10d is much larger and highly concentrated, with a higher 11 μm mean fire temperature (469.64 K). Therefore, this analysis confirms that fire pixels containing high temperature, large, and highly concentrated regions of sub-pixel fire hot spots are likely to produce the most accurate retrieved fire areas, especially when located near the center of the pixel.

The comparisons in Figs. 9a–d and 10a–d show the individual indirect effects (not originating from input variables) on the sub-pixel retrieval. These results suggest that multiple factors, such as a lower confidence fire pixel with pixel-edge hot spots, contribute to the large variability observed in the retrieved pixel-level fire area. Therefore, to visualize an ideal situation for the sub-pixel retrieval, the low and medium confidence fire pixels are removed (Fig. 9e) and the resulting correlation between MODIS and AMS shows a slight

increase (R = 0.67). When the fire pixels with pixel-edge hot spots are also removed (Fig. 9f), the correlation becomes much stronger (R = 0.84) and the variability between MODIS and AMS is reduced. This suggests that the combination of lower confidence fire pixels, typically from small sub-pixel fires (Fig. 9a) and PSF effects (Fig. 9d), including the distribution of sub-pixel hot spots (Fig. 10a-d), have the largest indirect impact on the accuracy of the retrieval. Similar to Fig. 9a–d, the results in Fig. 9f show a relatively low bias, but this accuracy is obtained by excluding 45% of the available fire pixels. When considering global fire observations, many cases of low confidence pixels are likely to exist, especially in regions with agricultural burning, and real-world applications would not be able to separate pixel-center from pixel-edge sub-pixel fires.

6.2. Clustering-level comparisons

While the AMS initial assessment algorithm enables the identification of fire pixels that have the greatest uncertainty in the retrieval, the majority of the future applications of the sub-pixel algorithm will not have these data available. Therefore, the sub-pixel retrieval will have to rely on a clustering methodology to increase the accuracy of the retrieved fire area. The results from the two clustering methods (Fig. 11) show stronger agreement than the pixel-level results. The clustering sum method of pixel-level retrievals produces the highest correlation (R = 0.91) suggesting that the random variation can be reduced by averaging, when looking at a fire event as a whole. The single retrieval method from averages also produces a high correlation (R = 0.84), but may be limited by the larger surface area used in the retrieval, where the contrast between fire and background may be reduced. Regardless, comparisons between the clustering and pixel-level results highlight the importance of averaging to reduce errors that are difficult to characterize on a per-pixel basis, such as the distribution of sub-pixel fires (Fig. 10a–d), general PSF effects (Fig. 9d), and PSF coregistration errors.

The fire clusters in Fig. 11 are currently defined as all MODIS pixels within an AMS scan, allowing for only six fire clusters and creating difficulty when discerning any impact from VZA and day/night cases. However, as with the pixel-level results, the larger VZA clusters generally display larger retrieved fire areas than the small VZA cases with a small bias toward larger AMS fire areas. Both clustering methodologies will likely improve estimates of retrieved fire area for large fire events, but future implementation of the single retrieval from averages method will require a strict definition of what constitutes a cluster in any given MODIS granule. Therefore, the sum of pixel-level retrievals method may be more advantageous because the definition of a cluster can be changed as needed. Unfortunately, isolated, small fires may only include one or two fire pixels and will not benefit from either clustering methodology.

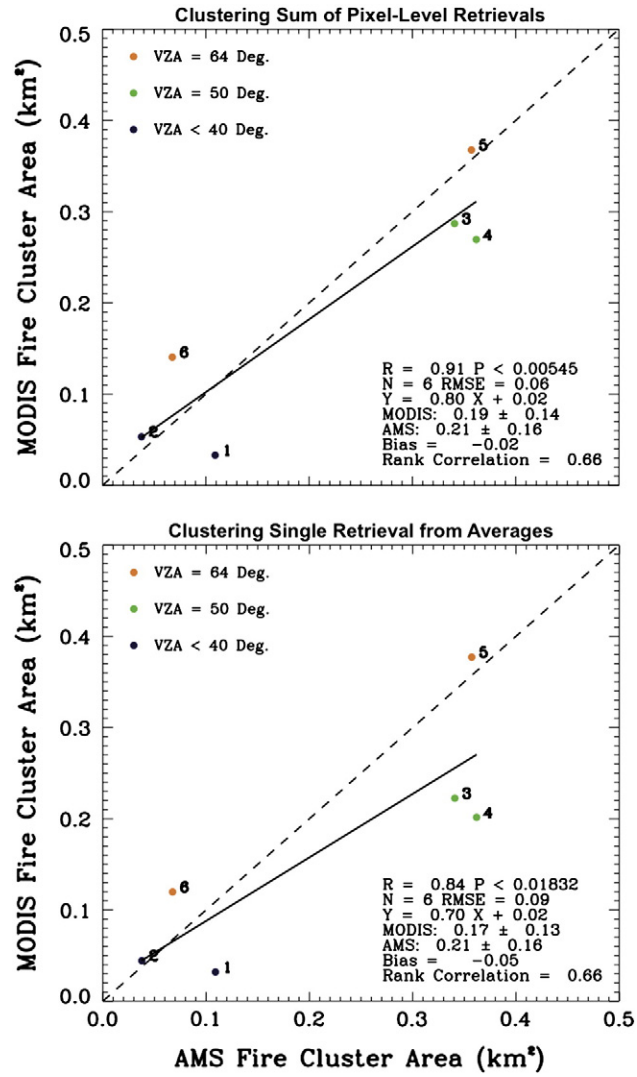

Fig. 11. Cluster-level comparisons between retrieved MODIS fire area and AMS observed fire area for all six collocated cases. (Top) Clustering using the sum of pixel-level retrievals method. (Bottom) Clustering using the single retrieval from averages method. Solid line corresponds to the linear fit equation and collocation case labels correspond to the first column of Table. 1. The color scheme is based on the viewing zenith angle (distance from nadir).

7. Comparing the sub-pixel-based FRP_f with the current MODIS FRP_p

With saturation occurring at higher temperatures in the AMS 4 μm channel, and thus providing very little data to validate retrieved fire temperatures, the comparison between the current MODIS FRP_p and FRP_f is the only available method to assess the overall consistency of MODIS sub-pixel fire retrievals. The pixel-level comparisons from all 6 collocation cases (Fig. 12a) produce a strong correlation (R = 0.93), which suggests that the sub-pixel retrieval can generate acceptable fire temperatures, even at the pixel level. However, the sensitivity analysis for the BIRD satellite (e.g. Zhukov et al., 2006) showed that the errors in retrieved fire area and temperature may counteract each other in a sub-pixel-based FRP calculation (Eq. 2). As a result, fire temperature errors may be present regardless of the accuracy in the retrieved fire area. When considering this dilemma and the lack of temperature validation data, the retrieved fire temperature should be used with caution, and only when FRP_f is not sufficient to examine the problem of interest.

In contrast to the fire area results in the previous sections, Fig. 12b shows that the off-nadir pixels (large VZAs) commonly have a much larger difference between FRP_p and FRP_f than cases close to nadir (small VZAs). The reason stems from the best-fit methodology of the MODIS FRP_p in combination with off-nadir pixel growth. For example, the size of the MODIS pixels displayed in Fig. 8 can grow to over 8 km^2 near the edge of the satellite ground swath (cases #5 and #6). In these cases, the background region of the pixel becomes very large, suggesting that the flaming region will contribute less to the observed pixel radiance. The FRP_p is also based on a top-of-atmosphere observation and the longer path lengths at large VZAs may mask the signal of fires. As a result, FRP_p will likely be much lower than FRP_f, which is indeed observed in most off-nadir pixels in Fig. 12a,b. Similarly, when FRP_p is divided by the pixel area, lower values (large-area pixels) will result in a greater potential for error in the MODIS FRP_p estimate. Therefore, with atmospheric effects taken into consideration, FRP_f is likely an

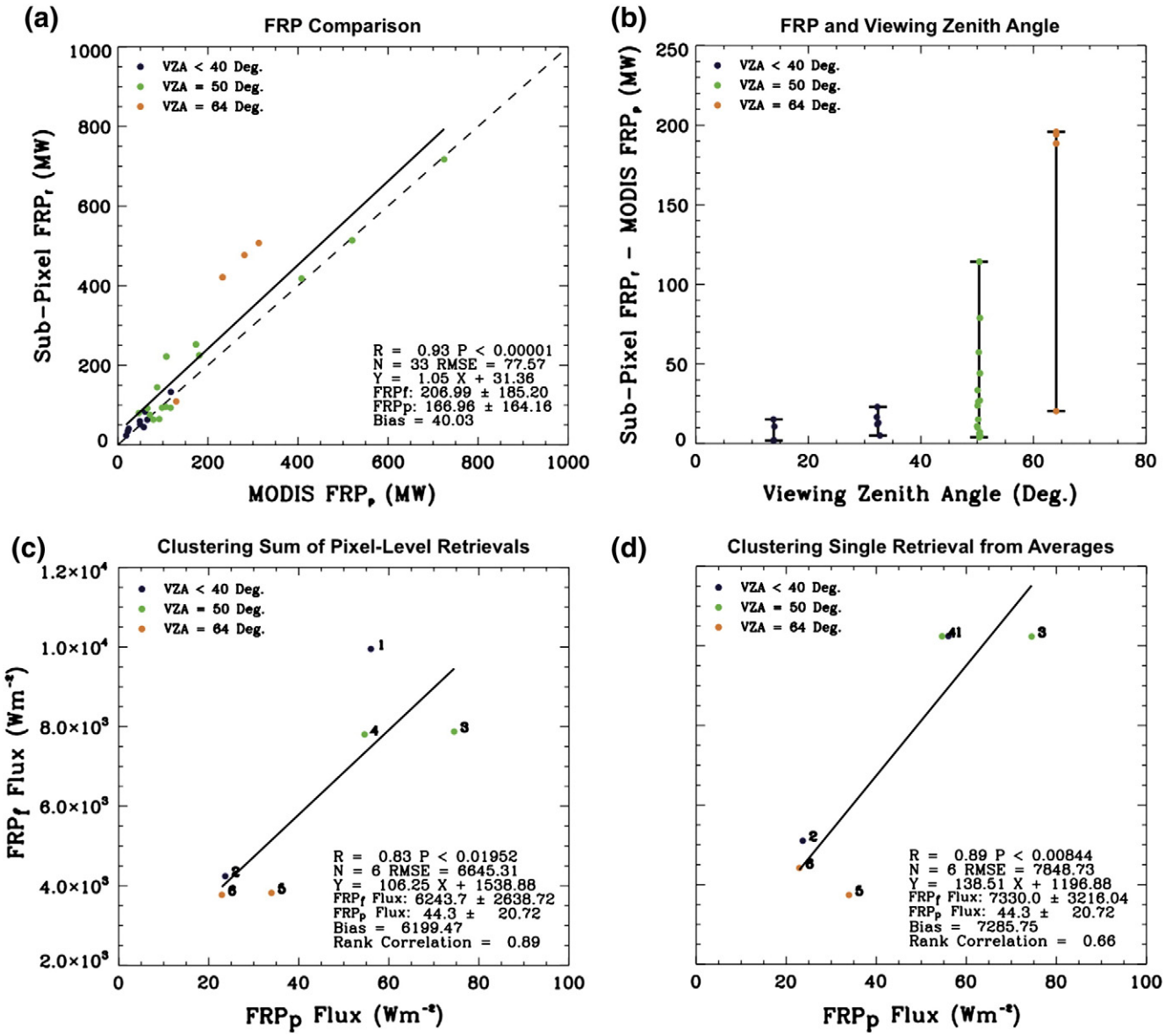

Fig. 12. (a) Pixel-level comparison between FRP_p (Current MODIS pixel-based FRP) and FRP_f (sub-pixel-based FRP) for all six cases. Solid line corresponds to the linear fit equation. (b) $FRP_f - FRP_p$ as a function of viewing zenith angle. (c) Cluster-level comparison between FRP_p per cluster area (FRP_p flux) and FRP_f per fire area (FRP_f flux) for all six cases using the sum of pixel-level retrievals method. (d) Same as (c) but for the single retrieval from averages method. Solid line corresponds to the linear fit equation and collocation case labels correspond to the first column of Table. 1. The color scheme is based on the viewing zenith angle (distance from nadir).

improved methodology for off-nadir fire pixels, but produces results similar to FRP_p for the remaining pixels.

The real motivation for choosing FRP_f over FRP_p becomes obvious when FRP_f is used in combination with the retrieved fire cluster area. This can be illustrated by comparing the cluster-level FRP_p flux to the FRP_f flux, given by

$$FRP_p\text{Flux} = \frac{\sum_{i=1}^{n} FRP_{p_i}}{\sum_{i=1}^{n} A_{p_i}} \tag{9}$$

$$FRP_f Flux = \frac{\sum_{i=1}^{n} FRP_{f_i}}{\sum_{i=1}^{n} A_{f_i}} \tag{10}$$

where the output is provided in units of Wm^{-2} per fire pixel cluster (Fig. 12c,d). The FRP_f flux and FRP_p flux are strongly correlated for both the sum method (R = 0.83) and the single retrieval method (R = 0.89). Furthermore, a strong rank correlation ($R_{rank\ sum} = 0.89$ and $R_{rank\ single} = 0.66$) suggests that there is a strong monotonically increasing relationship between the FRP_f and FRP_p fluxes. While limited by a small sample size, Fig. 12c,d shows that the magnitude of FRP_f flux ranges from ~3000 to 10,000 Wm^{-2}, and the FRP_P flux ranges from ~20 to 80 Wm^{-2}. Obviously, the magnitude of the FRP_f flux (based on retrieved fire area) is more realistic for the large fire clusters used in this study.

Along with an improved quantification of fire intensity, FRP_f flux can be used to examine the basic properties of a fire event by differentiating large fires burning at a low FRP_f from small fires burning at a high FRP_f. For example, the cluster fire area in case #5 is one of the largest (~0.38 km^2), while the FRP_f flux is one of the smallest (~3900 Wm^{-2}). In fact, both large VZA cases (#5 and #6) have the smallest FRP_f fluxes, which are expected because they are nighttime

cases. Therefore, the general fire evolution and smoke plume characteristics in case #5 may be considerably different than case #1, which contains a relatively small fire cluster area (~0.01 km^2) with a much larger FRP_f flux (~10,000 Wm^{-2}). These types of comparisons demonstrate the potential utility of the sub-pixel retrieval for providing a detailed characterization of any given fire event, and show that FRP_f flux may be useful for providing improved estimates of initial smoke plume buoyancy and injection heights. However, more observational analysis is needed to support this hypothesis.

8. Summary and applications to future satellite missions

In an effort to provide a fire area and temperature-based FRP product, this study has developed a MODIS sub-pixel retrieval algorithm for fire area and temperature, which are used to calculate FRP_f and FRP_f flux. The retrieval was designed such that it can be run on any MODIS granule across the globe and a radiative transfer model was used to account for atmospheric effects. Using a lookup table approach, the retrieval can be run at both the pixel and cluster levels and corrections are made for overlapping pixels. Currently, the 4 and 11 μm background temperatures are direct inputs from the MODIS fire product (collection 5).

For the first time, the AMS sensor, flown aboard the NASA Ikhana UAS, allowed the retrieved MODIS sub-pixel fire area results to be assessed using high spatial resolution data. This initial assessment showed that pixel clustering should be implemented to reduce errors that are difficult to characterize on a per-pixel basis, such as those from PSF differences, and the clustering sum of individual retrievals method may have the greatest relevance to future operational algorithms. In addition, a strong correlation ($R = 0.93$) was found between the fire area/temperature-based FRP_f and the current pixel-based MODIS FRP_p. This suggests that a sub-pixel retrieval of FRP_f has the same merit as the current FRP_p, but contributes information that the current MODIS product is lacking. As an example, the combination of FRP_f and retrieved fire area (FRP_f flux) may offer a reliable characterization of thermal buoyancy for estimates of smoke plume height, at least for medium to large fires (>1000 m^2). Improved plume height estimates have the most value for these large fire events due to the increased chance of injection above the boundary layer.

Over the next decade, the new generation of satellite sensors, such as VIIRS (http://jointmission.gsfc.nasa.gov/viirs.html) and GOES-R (http://www.goes-r.gov/), will replace the current generation sensors, including MODIS. The sub-pixel algorithm described in this paper is designed for easy application to these future sensors, provided the basic spectral properties are similar. The VIIRS and GOES-R fire detection algorithms, currently being designed and evaluated, will perform sub-pixel fire characterization (e.g. Schmidt et al., 2011). However, in contrast to MODIS, the VIIRS sensor will provide a finer pixel resolution of about 750 m across the entire scan (nadir and off-nadir), reducing off-nadir pixel growth (Csiszar et al., 2011), and thereby enhancing any potential FRP_f product. If the sub-pixel algorithm developed in this study becomes operational, the approximate size of the fire front could be calculated at each observation time, which will facilitate the analysis of meteorological impacts on fire intensity, size, and temperature (e.g. Peterson et al., 2010). From the operational perspective, there is a growing need for a near-real-time fire intensity rating system (Ichoku et al., 2008a). The incorporation of FRP_f will allow future fire-rating techniques to include aspects of fire front size, which will likely help fire suppression teams to allocate their resources more efficiently during a fire emergency.

The initial assessment methodology for the MODIS sub-pixel retrieval can also be applied to future studies. In fact, as sub-pixel retrievals are incorporated into operational satellite missions, increasing quantities of high-resolution validation data will be required. This highlights the value of airborne-sensor-collected fire data, such as those obtained from the AMS sensor aboard NASA's Ikhana aircraft. Currently, the Ikhana is flown over large fire events to support fire suppression operations on the ground. However, these flights also have an enormous scientific value for understanding wildfire behavior and are a potential tool for the direct validation of FRP_f. This study has shown that the greatest potential for error occurs with small sub-pixel fires, but validation data for these events are not currently available. Therefore, future airborne missions must focus on data collection for both large and small fire events over a wide variety of biomass types.

Acknowledgments

We are grateful to the AMS wildfire measurement team at the NASA Ames Research Center for providing the airborne (AMS) fire data used in this study. We thank Luke Ellison at the NASA Goddard Space Flight Center for his work with overlapping MODIS pixels. We also thank Dr. Mark Anderson, Dr. John Lenters, and Dr. Bob Oglesby at the University of Nebraska — Lincoln and Dr. Wilfrid Schroeder at the University of Maryland — College Park for their constructive comments. The project was funded by the NASA Earth and Space Science Fellowship (to D. Peterson) and the NASA New Investigator Program (to Dr. Jun Wang). Dr. Hyer's participation was funded by NASA Applied Science award #NNX09AT09G and NASA R&A award #NNH07AF47I.

References

Ambrosia, V. G., Sullivan, D. V., & Buechel, S. (2011). Integrating sensor data and geospatial tools to enhance real-time disaster management capabilities: Wildfire observations. In A. K. Sinha, D. Arctur, I. Jackson, & L. Gundersen (Eds.), *Societal challenges and geoinformatics: Geological society of America special paper*, *482*. (pp. 1–12)Boulder, CO: The Geological Society of America978-0-8137-2482-9 ((pbk), Chapter 1).

Ambrosia, V. G., & Wegener, S. (2009). Unmanned airborne platforms for disaster remote sensing support. In Pei-Gee Peter Ho (Ed.), *Geoscience and remote sensing. InTech*. (pp. 91–114)978-953-307-003-2 (Chapter 5).

Ambrosia, V. G., Wegener, S., Zajkowski, T., Sullivan, D. V., Buechel, S., Enomoto, F., et al. (2011). The Ikhana UAS western states fire imaging missions: From concept to reality (2006–2010). *Geocarto International Journal*, *26*. (pp. 85–101): Taylor & Francis Publishing.

Byram, G. M. (1959). Combustion of forest fuels. In K. P. Davis (Ed.), *Forest fire: Control and use* (pp. 61–89). New York: McGraw-Hill.

Cahoon, D. R., Jr., Stocks, B. J., Levine, J. S., Cofer, W. R., III, & Chung, C. C. (1992). Evaluation of a technique for satellite-derived area estimation of forest fires. *Journal of Geophysical Research*, *97*, 805–3814.

Calle, A., Casanova, J. L., & Gonzalez-Alonso, F. (2009). Impact of point spread function of MSG-SEVIRI on active fire detection. *International Journal of Remote Sensing*, *30*, 4567–4579.

Csiszar, I. A., Schroeder, W., Giglio, L., Justice, C. O., & Ellicott, E. (2011). Quantitative evaluation of active fire detection capabilities from VIIRS. *91st American Meteorological Society Annual Meeting. Seattle, WA*.

Dennison, P. E., Charoensiri, K., Roberts, D. A., Peterson, S. H., & Green, R. O. (2006). Wildfire temperature and land cover modeling using hyperspectral data. *Remote Sensing of Environment*, *100*, 212–222.

Dozier, J. (1981). A method for satellite identification of surface temperature fields of subpixel resolution. *Remote Sensing of Environment*, *11*, 221–229.

Duck, T. J., Firanski, B. J., Millet, D. B., Goldstein, A. H., Allan, J., Holzinger, R., et al. (2007). Transport of forest fire emissions from Alaska and the Yukon Territory to Nova Scotia during summer 2004. *Journal of Geophysical Research-Atmospheres*, *112*.

Eckmann, T. C., Roberts, D. A., & Still, C. J. (2008). Using multiple endmember spectral mixture analysis to retrieve subpixel fire properties from MODIS. *Remote Sensing of Environment*, *112*, 3773–3783.

Eckmann, T. C., Roberts, D. A., & Still, C. J. (2009). Estimating subpixel fire sizes and temperatures from ASTER using multiple endmember spectral mixture analysis. *International Journal of Remote Sensing*, *30*, 5851–5864.

Eckmann, T. C., Still, C. J., Roberts, D. A., & Michaelsen, J. C. (2010). Variations in subpixel fire properties with season and land cover in Southern Africa. *Earth Interactions*, *14*.

Filippi, J. B., Bosseur, F., Mari, C., Lac, C., Le Moigne, P., Cuenot, B., et al. (2009). Coupled atmosphere—Wildland fire modelling. *Journal of Advances in Modeling Earth Systems*, *1*, 1–9.

Flannigan, M. D., & Vonder Haar, T. H. (1986). Forest fire monitoring using NOAA satellite AVHRR. *Canadian Journal of Forest Research*, *16*, 975–982.

Flasse, S. P., & Ceccato, P. S. (1996). A contextual algorithm for AVHRR fire detection. *International Journal of Remote Sensing*, *17*, 419–424.

Fromm, M., Lindsey, D. T., Servranckx, R., Yue, G., Trickl, T., Sica, R., et al. (2010). The untold story of pyrocumulonimbus. *Bulletin of the American Meteorological Society*, *91*, 1193–1209.

Gao, B. C., Xiong, X. X., Li, R. R., & Wang, D. Y. (2007). Evaluation of the moderate resolution imaging spectrometer special 3.95-mu m fire channel and implications on fire channel selections for future satellite instruments. *Journal of Applied Remote Sensing*, *1*.

Giglio, L. (2010). MODIS collection 5 active fire product user's guide version 2.4. *University of Maryland, Department of Geography* (pp. 1–61).
Giglio, L., Descloitres, J., Justice, C. O., & Kaufman, Y. J. (2003). An enhanced contextual fire detection algorithm for MODIS. *Remote Sensing of Environment*, *87*, 273–282.
Giglio, L., & Justice, C. O. (2003). Effect of wavelength selection on characterization of fire size and temperature. *International Journal of Remote Sensing*, *24*, 3515–3520.
Giglio, L., & Kendall, J. D. (2001). Application of the Dozier retrieval to wildfire characterization — A sensitivity analysis. *Remote Sensing of Environment*, *77*, 34–49.
Giglio, L., Kendall, J. D., & Justice, C. O. (1999). Evaluation of global fire detection algorithms using simulated AVHRR infrared data. *International Journal of Remote Sensing*, *20*, 1947–1985.
Gomez-Landesa, E., Rango, A., & Bleiweiss, M. (2004). An algorithm to address the MODIS bowtie effect. *Canadian Journal of Remote Sensing*, *30*, 644–650.
Green, R. O. (1996). Estimation of biomass fire temperature and areal extent from calibrated AVIRIS spectra. *Summaries of the sixth annual JPL airborne earth science workshop*, *96–4, 1*. (pp. 105–113): JPL Publication.
Hyer, E. J., & Reid, J. S. (2009). Baseline uncertainties in biomass burning emission models resulting from spatial error in satellite active fire location data. *Geophysical Research Letters*, *36*.
Ichoku, C., Giglio, L., Wooster, M. J., & Remer, L. A. (2008). Global characterization of biomass-burning patterns using satellite measurements of fire radiative energy. *Remote Sensing of Environment*, *112*, 2950–2962.
Ichoku, C., & Kaufman, Y. J. (2005). A method to derive smoke emission rates from MODIS fire radiative energy measurements. *IEEE Transactions on Geoscience and Remote Sensing*, *43*, 2636–2649.
Ichoku, C., Martins, J. V., Kaufman, Y. J., Wooster, M. J., Freeborn, P. H., Hao, W. M., et al. (2008). Laboratory investigation of fire radiative energy and smoke aerosol emissions. *Journal of Geophysical Research-Atmospheres*, *113*.
Jordan, N. S., Ichoku, C., & Hoff, R. M. (2008). Estimating smoke emissions over the US Southern Great Plains using MODIS fire radiative power and aerosol observations. *Atmospheric Environment*, *42*, 2007–2022.
Justice, C. O., Giglio, L., Korontzi, S., Owens, J., Morisette, J. T., Roy, D., et al. (2002). The MODIS fire products. *Remote Sensing of Environment*, *83*, 244–262.
Kahn, R. A., Li, W. H., Moroney, C., Diner, D. J., Martonchik, J. V., & Fishbein, E. (2007). Aerosol source plume physical characteristics from space-based multiangle imaging. *Journal of Geophysical Research-Atmospheres*, *112*, 20.
Kaiser, J. W., Suttie, M., Flemming, J., Morcrette, J. J., Boucher, O., & Schultz, M. G. (2009). Global real-time fire emission estimates based on space-borne fire radiative power observations. *ECMWF and AER* (pp. 1–4).
Kaufman, Y. J., Ichoku, C., Giglio, L., Korontzi, S., Chu, D. A., Hao, W. M., et al. (2003). Fire and smoke observed from the Earth Observing System MODIS instrument — Products, validation, and operational use. *International Journal of Remote Sensing*, *24*, 1765–1781.
Kaufman, Y. J., Justice, C. O., Flynn, L. P., Kendall, J. D., Prins, E. M., Giglio, L., et al. (1998). Potential global fire monitoring from EOS-MODIS. *Journal of Geophysical Research-Atmospheres*, *103*, 32215–32238.
Kaufman, Y. J., Kleidman, R. G., & King, M. D. (1998). SCAR-B fires in the tropics: Properties and remote sensing from EOS-MODIS. *Journal of Geophysical Research-Atmospheres*, *103*, 31955–31968.
Kelha, V., Rauste, Y., Hame, T., Sephton, T., Buongiorno, A., Frauenberger, O., et al. (2003). Combining AVHRR and ATSR satellite sensor data for operational boreal forest fire detection. *International Journal of Remote Sensing*, *24*, 1691–1708.
Kopacz, M., Mauzerall, D. L., Wang, J., Leibensperger, E. M., Henze, D. K., & Singh, K. (2011). Origin and radiative forcing of black carbon transported to the Himalayas and Tibetan Plateau. *Atmospheric Chemistry and Physics*, *11*, 2837–2852.
Koren, I., Remer, L. A., & Longo, K. (2007). Reversal of trend of biomass burning in the Amazon. *Geophysical Research Letters*, *34*.
Langaas, S. (1993). A parameterized bispectral model for savannah fire detection using AVHRR night images. *International Journal of Remote Sensing*, *14*, 2245–2262.
Lavoue, D., Liousse, C., Cachier, H., Stocks, B. J., & Goldammer, J. G. (2000). Modeling of carbonaceous particles emitted by boreal and temperate wildfires at northern latitudes. *Journal of Geophysical Research-Atmospheres*, *105*, 26871–26890.
Lee, T. F., & Tag, P. M. (1990). Improved detection of hotspots using the AVHRR 3.7-um channel. *Bulletin of the American Meteorological Society*, *71*, 1722–1730.
Li, Z., Kaufman, Y., Ichoku, C., Fraser, R., Trishchenko, A., Giglio, L., et al. (2001). A review of AVHRR-based active fire detection algorithms: Principles, limitations, and recommendations. In F. Ahern, J. Goldammer, & C. O. Juctice (Eds.), *Global and regional vegetation fire monitoring from space: planning a coordinated international effort* (pp. 199–225). : SPB Academic Publishing.
Li, Z., Nadon, S., & Cihlar, J. (2000). Satellite detection of Canadian boreal forest fires: development and application of an algorithm. *International Journal of Remote Sensing*, *21*, 3057–3069.
Li, Z., Nadon, S., Cihlar, J., & Stocks, B. (2000). Satellite mapping of Canadian boreal forest fires: Evaluation and comparison of algorithms. *International Journal of Remote Sensing*, *21*, 3071–3082.
Masuoka, E., Fleig, A., Wolfe, R. E., & Patt, F. (1998). Key characteristics of MODIS data products. *IEEE Transactions on Geoscience and Remote Sensing*, *36*, 1313–1323.
Matson, M., & Dozier, J. (1981). Identification of subresolution high temperature sources using a thermal IR sensor. *Photogrammetric Engineering and Remote Sensing*, *47*, 1311–1318.
Mell, W., Jenkins, M. A., Gould, J., & Cheney, P. (2007). A physics-based approach to modelling grassland fires. *International Journal of Wildland Fire*, *16*, 1–22.
Oertel, D., Zhukov, B., Thamm, H. P., Roehrig, J., & Orthmann, B. (2004). Space-borne high resolution fire remote sensing in Benin, West Africa. *International Journal of Remote Sensing*, *25*, 2209–2216.
Peterson, D., Wang, J., Ichoku, C., & Remer, L. A. (2010). Effects of lightning and other meteorological factors on fire activity in the North American boreal forest: Implications for fire weather forecasting. *Atmospheric Chemistry and Physics*, *10*, 6873–6888.
Petitcolin, F., & Vermote, E. (2002). Land surface reflectance, emissivity and temperature from MODIS middle and thermal infrared data. *Remote Sensing of Environment*, *83*, 112–134.
Prins, E. M., & Menzel, W. P. (1992). Geostationary satellite detection of biomass burning in South-America. *International Journal of Remote Sensing*, *13*, 2783–2799.
Prins, E. M., & Menzel, W. P. (1994). Trends in South-American biomass burning detected with the GOES Visible Infrared Spin Scan Radiometer Atmospheric Sounder from 1983 to 1991. *Journal of Geophysical Research-Atmospheres*, *99*, 16719–16735.
Randerson, J. T., Liu, H., Flanner, M. G., Chambers, S. D., Jin, Y., Hess, P. G., et al. (2006). The impact of boreal forest fire on climate warming. *Science*, *314*, 1130–1132.
Ricchiazzi, P., Yang, S. R., Gautier, C., & Sowle, D. (1998). SBDART: A research and teaching software tool for plane-parallell radiative transfer in the Earth's atmosphere. *Bulletin of the American Meteorological Society*, *79*, 2101–2114.
Riggan, P. J., Brass, J. A., & Lockwood, R. N. (1993). Assessing fire emissions from tropical savanna and forests of central Brazil. *Photogrammetric Engineering and Remote Sensing*, *59*, 1009–1015.
Roberts, G., Wooster, M. J., & Lagoudakis, E. (2009). Annual and diurnal african biomass burning temporal dynamics. *Biogeosciences*, *6*, 849–866.
Roberts, G., Wooster, M. J., Perry, G. L. W., Drake, N., Rebelo, L. M., & Dipotso, F. (2005). Retrieval of biomass combustion rates and totals from fire radiative power observations: Application to southern Africa using geostationary SEVIRI imagery. *Journal of Geophysical Research-Atmospheres*, *110*.
Roy, D. P., Boschetti, L., Justice, C. O., & Ju, J. (2008). The collection 5 MODIS burned area product — Global evaluation by comparison with the MODIS active fire product. *Remote Sensing of Environment*, *112*, 3690–3707.
Sapkota, A., Symons, J. M., Kleissl, J., Wang, L., Parlange, M. B., Ondov, J., et al. (2005). Impact of the 2002 Canadian forest fires on particulate matter air quality in Baltimore City. *Environmental Science & Technology*, *39*, 24–32.
Schmidt, C. C., Hoffman, J. P., & Prins, E. M. (2011). Detection and characterization of biomass burning in the GOES-R era. *91st American Meteorological Society Annual Meeting. Seattle, WA*.
Schroeder, W., Csiszar, I., Giglio, L., & Schmidt, C. C. (2010). On the use of fire radiative power, area, and temperature estimates to characterize biomass burning via moderate to coarse spatial resolution remote sensing data in the Brazilian Amazon. *Journal of Geophysical Research*, *115*, D21121.
Schroeder, W., Prins, E., Giglio, L., Csiszar, I., Schmidt, C., Morisette, J., et al. (2008). Validation of GOES and MODIS active fire detection products using ASTER and ETM plus data. *Remote Sensing of Environment*, *112*, 2711–2726.
Shephard, M. W., & Kennelly, E. J. (2003). Effect of band-to-band coregistration on fire property retrievals. *IEEE Transactions on Geoscience and Remote Sensing*, *41*, 2648–2661.
Spracklen, D. V., Logan, J. A., Mickley, L. J., Park, R. J., Yevich, R., Westerling, A. L., et al. (2007). Wildfires drive interannual variability of organic carbon aerosol in the western US in summer. *Geophysical Research Letters*, *34*.
Stephens, S. L., Weise, D. R., Fry, D. L., Keiffer, R. J., Dawson, J., Koo, E., et al. (2008). Measuring the rate of spread of chaparral prescribed fires in northern California. *Fire Ecology*, *4*, 74–86.
Tang, B. -H., Li, Z. -L., & Bi, Y. (2009). Estimation of land surface directional emissivityin mid-infrared channel around 4.0 μm from MODIS data. *Optics Express*, *17*, 3173–3182.
Val Martin, M., Logan, J. A., Kahn, R. A., Leung, F. Y., Nelson, D. L., & Diner, D. J. (2010). Smoke injection heights from fires in North America: Analysis of 5 years of satellite observations. *Atmospheric Chemistry and Physics*, *10*, 1491–1510.
van der Werf, G. R., Randerson, J. T., Giglio, L., Gobron, N., & Dolman, A. J. (2008). Climate controls on the variability of fires in the tropics and subtropics. *Global Biogeochemical Cycles*, *22*.
Vermote, E., Ellicott, E., Dubovik, O., Lapyonok, T., Chin, M., Giglio, L., et al. (2009). An approach to estimate global biomass burning emissions of organic and black carbon from MODIS fire radiative power. *Journal of Geophysical Research*, *114*, D18205.
Wang, J., Christopher, S. A., Nair, U. S., Reid, J. S., Prins, E. M., Szykman, J., et al. (2006). Mesoscale modeling of Central American smoke transport to the United States: 1. "Top-down" assessment of emission strength and diurnal variation impacts. *Journal of Geophysical Research-Atmospheres*, *111*.
Westerling, A. L., Gershunov, A., Brown, T. J., Cayan, D. R., & Dettinger, M. D. (2003). Climate and wildfire in the western United States. *Bulletin of the American Meteorological Society*, *84*, 595–604.
Wolfe, R. E., Nishihama, M., Fleig, A. J., Kuyper, J. A., Roy, D. P., Storey, J. C., et al. (2002). Achieving sub-pixel geolocation accuracy in support of MODIS land science. *Remote Sensing of Environment*, *83*, 31–49.
Wooster, M. J. (2002). Small-scale experimental testing of fire radiative energy for quantifying mass combusted in natural vegetation fires. *Geophysical Research Letters*, *29*.
Wooster, M. J., Roberts, G., Perry, G. L. W., & Kaufman, Y. J. (2005). Retrieval of biomass combustion rates and totals from fire radiative power observations: FRP derivation and calibration relationships between biomass consumption and fire radiative energy release. *Journal of Geophysical Research-Atmospheres*, *110*.
Wooster, M. J., Zhukov, B., & Oertel, D. (2003). Fire radiative energy for quantitative study of biomass burning: Derivation from the BIRD experimental satellite and comparison to MODIS fire products. *Remote Sensing of Environment*, *86*, 83–107.
Zhukov, B., Briess, K., Lorenz, E., Oertel, D., & Skrbek, W. (2005). Detection and analysis of high-temperature events in the BIRD mission. *Acta Astronautica*, *56*, 65–71.
Zhukov, B., Lorenz, E., Oertel, D., Wooster, M., & Roberts, G. (2006). Spaceborne detection and characterization of fires during the bi-spectral infrared detection (BIRD) experimental small satellite mission (2001–2004). *Remote Sensing of Environment*, *100*, 29–51.